



BANGLADESH UNIVERSITY OF ENGINEERING AND TECHNOLOGY

**ANALYSIS OF BIMETALLIC NANOROD  
DIMER BIOSENSORS FOR LABEL-FREE  
MOLECULE DETECTION**

*by*

**Avijit Das**

Student ID: 1014062255 P

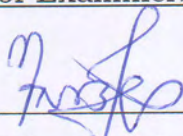
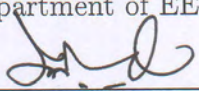
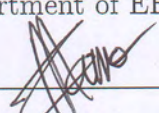
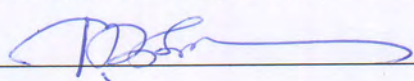
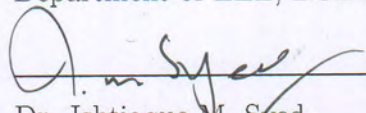
*A thesis submitted in partial fulfillment of the requirements  
for the degree of Masters of Science  
in the  
Department of Electrical and Electronic Engineering*

August 2016

# Approval

This thesis titled “ANALYSIS OF BIMETALLIC NANOROD DIMER BIOSENSORS FOR LABEL-FREE MOLECULE DETECTION” submitted by Avijit Das, Student No: 1014062255 P, Session: October/2014, has been accepted as satisfactory in partial fulfillment of the requirements for the degree of Master of Science in Electrical and Electronic Engineering on August 29, 2016.

## Board of Examiners:

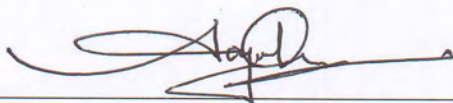
1.   
\_\_\_\_\_  
Dr. Muhammad Anisuzzaman Talukder  
Professor  
Department of EEE, BUET, Dhaka.  
Chairman  
(Supervisor)
2.   
\_\_\_\_\_  
Dr. Quazi Deen Mohd Khosru  
Professor and Head  
Department of EEE, BUET, Dhaka.  
Member  
(Ex-Officio)
3.   
\_\_\_\_\_  
Dr. Sharif Mohammad Mominuzzaman  
Professor  
Department of EEE, BUET, Dhaka.  
Member
4.   
\_\_\_\_\_  
Dr. Md. Zahurul Islam  
Associate Professor  
Department of EEE, BUET, Dhaka.  
Member
5.   
\_\_\_\_\_  
Dr. Ishtiaque M. Syed  
Professor  
Department of Physics, University of Dhaka, Dhaka-1000.  
Member  
(External)

## Declaration of Authorship

I, Avijit Das, declare that this thesis titled, "ANALYSIS OF BIMETALLIC NANOROD DIMER BIOSENSORS FOR LABEL-FREE MOLECULE DETECTION" and the work presented in it are my own. I confirm that:

- This work was done wholly or mainly while in candidature for a degree at this University.
- Where I have consulted the published work of others, this is always clearly attributed.
- Where I have quoted from the work of others, the source is always given. With the exception of such quotations, this thesis is entirely my own work.
- I have acknowledged all main sources of help.

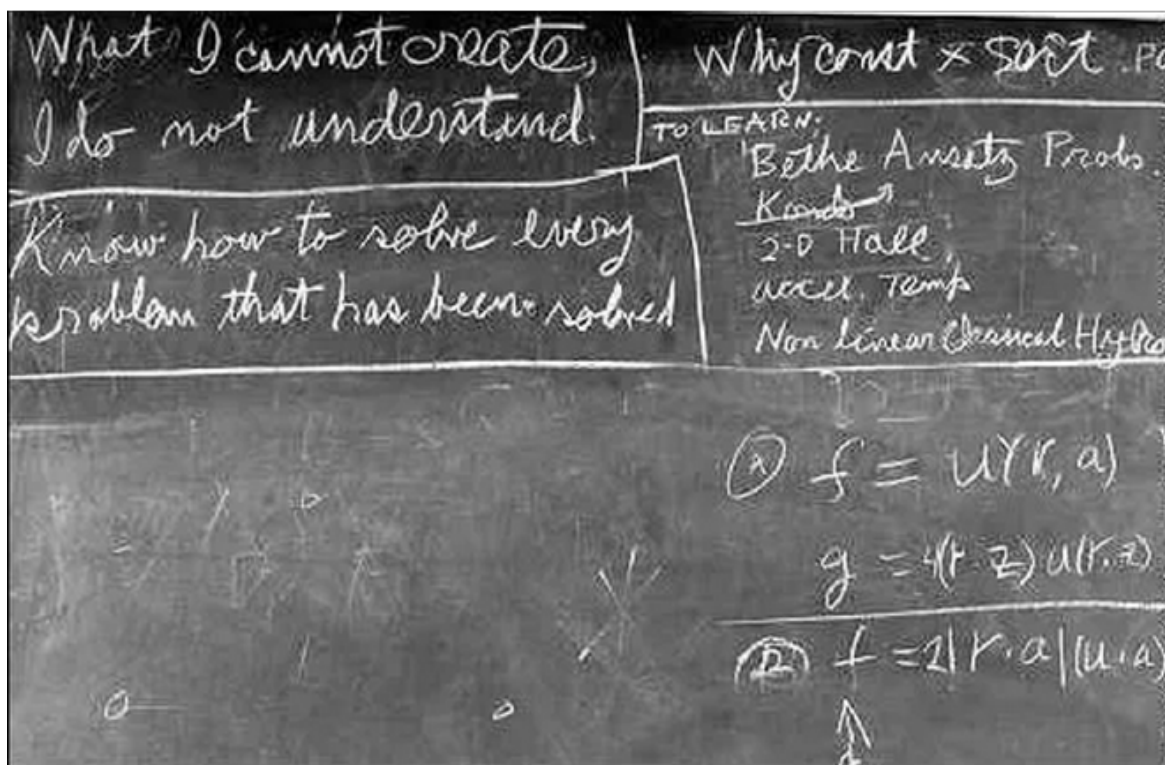
Signed:



---

(Avijit Das)

This inspiring words are seared in the DNA code of the first man made synthetic life Mycoplasma laboratorium by Craig Venter, 2010), and is the foundation of our research philosophy.



'What I cannot create, I do not understand.' - on Richard Feynman's blackboard at the time of his death in February 1988.

# Abstract

A bimetallic nanorod dimer biosensor based on localized surface plasmon resonance (LSPR) has been proposed in this thesis. Larger absorption and stronger electric field coupling have been achieved when a gold (Au) core nanorod is coated with silver (Ag) shell layer (Au@Ag). The optical response, e.g., dielectric function of this bimetallic monomer has been modeled analytically with the help of Clausius-Mossotti equation. Using the developed model, the polarizability, dipole moment, and absorption cross-section of the Au@Ag nanorod dimer have been calculated. In order to investigate the molecular sensitivity, this bimetallic dimer has been simulated without and with the presence of label-free proteins using the finite difference time domain (FDTD) technique. Lysozyme (Lys), human serum albumin (HSA), human  $\gamma$ -immunoglobulin (IgG), adenomatous polyposis coli (APC) and human fibrinogen (Fb) proteins have been used to calculate the resonance shifts from the FDTD simulations. In addition, effects of physical parameters, orientations and environment of Au@Ag nanorods in the dimer system have also been studied through peak shifts for an APC protein sample. The shift values from the proposed structure have been found to be 6%–30% larger compared to the conventionally used Au dimer sensors. Therefore, better sensitivity performance of the Au@Ag nanorod dimers would pave the way for its extensive research in biochemical and pharmaceutical industries.

# Acknowledgement

This note is made to express my gratefulness to some people who really encouraged and supported me a lot in making this report.

First of all, my sincere most thanks go to Dr. Muhammad Anisuzzaman Talukder , my respected supervisor of thesis who appreciated the idea of doing needs analysis on reading skills. He has always been highly kind and patient in making me aware of every possible problem that I might encounter while dealing with this issue. The necessary instructions and materials provided by him literally helped me a lot to understand the situation better and analyze it effectively. Without his keen supervision, it was virtually impossible for me to finish this report successfully in time.

I would like to offer my thanks to my fellow researcher Zabir Ahmed who advised me in critical situations for understanding the relevant topics. A note of acknowledgement must also go out to my research lab partners Md. Rifat Kaiser Rachi and Raiyan Abdul Baten, it was an honor to have such intelligent and friendly company during my research.

Last but not the least; I am very grateful to the Almighty, who has blessed me with knowledge and ability to write this report successfully.

# Contents

<b>Approval</b>	<b>i</b>
<b>Declaration of Authorship</b>	<b>ii</b>
<b>Abstract</b>	<b>iv</b>
<b>Acknowledgement</b>	<b>v</b>
<b>List of Figures</b>	<b>ix</b>
<b>1 Introduction</b>	<b>1</b>
1.1 Nanoplasmonics . . . . .	1
1.2 Nanoplasmonic Sensing . . . . .	3
1.3 Biomolecule Detection: Present State of the Problem . . . . .	4
1.4 Overview of the Thesis . . . . .	5
<b>2 Physics of LSPR</b>	<b>6</b>
2.1 Bulk Surface and Localized Surface Plasmons . . . . .	6
2.2 Overview of Drude-Sommerfeld Theory . . . . .	8
2.3 Mie Theory . . . . .	10
2.4 Gans Theory . . . . .	12
2.5 Summary . . . . .	13
<b>3 Bimetallic Nanorod Dimer Biosensor</b>	<b>14</b>
3.1 Introduction . . . . .	14
3.2 Proposed Structure . . . . .	15
3.3 Protein as a Biomolecule . . . . .	16
3.3.1 Lysozyme (Lys) . . . . .	16
3.3.2 Human serum albumin (HSA) . . . . .	17

3.3.3	Human $\gamma$ -immunoglobulin (IgG)	18
3.3.4	Adenomatous polyposis coli (APC)	18
3.3.5	Human fibrinogen (Fb)	19
3.4	Summary	19
<b>4</b>	<b>Analytical Modeling of Bimetallic Dimer</b>	<b>20</b>
4.1	Introduction	20
4.2	Dielectric Function of an Au@Ag Nanorod	21
4.3	Plasmon Resonance Condition in Bimetallic Nanorod System	26
4.4	Bimetallic Nanorod Dimer	29
4.5	Summary	33
<b>5</b>	<b>FDTD Simulation</b>	<b>34</b>
5.1	Introduction	34
5.2	Material Modeling	35
5.3	Biomolecule Modeling	35
5.4	Mesh Independence Test	36
5.5	Boundary Conditions	37
5.5.1	Perfectly Matched Layers	37
5.5.2	Periodic	37
5.6	Optical Sources	38
5.7	Power Absorption	38
5.8	Summary	39
<b>6</b>	<b>Simulation and Result Analysis</b>	<b>40</b>
6.1	Introduction	40
6.2	Physical Parameters of Nanorod Monomers	41
6.2.1	Core-Shell Ratio	41
6.2.2	Aspect Ratio	45
6.3	Physical Orientation of Monomers in the Dimer	48
6.3.1	Nanorod Positions	48
6.3.2	Gap Width between Nanorods	51
6.4	Parameters in Physical Environment	52
6.4.1	Incident Angle of Light	52
6.4.2	Chaotropic Agents in Buffer Solution	54



6.5	Sensitivity Analysis for Different Proteins . . . . .	55
6.5.1	Effects of Size and Material . . . . .	55
6.5.2	Substrate Effect . . . . .	57
6.6	Summary . . . . .	58
<b>7</b>	<b>Conclusion and Future Works</b>	<b>59</b>
	<b>Bibliography</b>	<b>61</b>

# List of Figures

1.1	The Lycurgus cup illuminated with ambient lighting (left) and illuminated from inside (right) [7]. . . . .	2
2.1	Illustration of surface plasmons [46]. . . . .	7
2.2	Illustration of localized surface plasmons [47]. . . . .	7
3.1	Proposed Au@Ag nanorod dimer for biomolecule detection . . . . .	15
3.2	Ribbon model structure of lysozyme (Lys) protein . . . . .	17
3.3	Ribbon model structure of human serum albumin (HSA) protein . . . . .	17
3.4	Ribbon model structure of human $\gamma$ -immunoglobulin (IgG) protein . . . . .	18
3.5	Ribbon model structure of adenomatous polyposis coli (APC) protein . . . . .	18
3.6	Ribbon model structure of human fibrinogen (Fb)) protein . . . . .	19
4.1	The dipole equivalence principle scheme. (a) The initial Au nanorod (semimajor axis- $a_1$ , semiminor axis- $b_1$ and dielectric function, $\epsilon_{Au}$ ) covered by an outer Ag layer with thickness, $d$ and dielectric function, $\epsilon_{Ag}$ , in a surrounding medium of dielectric function, $\epsilon_m$ . (b) The initial Au nanorod in the dielectric medium of $\epsilon_{Ag}$ , surrounded by an imaginary coating of thickness, $d$ . (c) An equivalent nanorod with dielectric function of $\epsilon_{av}$ in the dielectric medium of $\epsilon_{Ag}$ . (d) The equivalent nanorod with semimajor axis- $a_2$ , semiminor axis- $b_2$ and dielectric function, $\epsilon_{av}$ in the surrounding medium of $\epsilon_m$ . . . . .	21
4.2	Real and imaginary parts of the dielectric function of Au@Ag nanorod system for different Ag shells $d$ . (a) Extended and (b) zoomed versions of the real parts $\epsilon_1$ with variation of $d$ . (c) Extended and (d) zoomed versions of the imaginary parts $\epsilon_2$ with variation of $d$ . . . . .	25
4.3	(a) Extended and (b) zoomed versions of energy loss function of the bimetallic nanorod system for different Ag shells $d$ . . . . .	26

4.4	Real (a) and imaginary (b) parts of the electron susceptibility of bimetallic nanorod system for different Ag shells $d$ . . . . .	29
4.5	Schematic representation of the coordinate system employed in the derivation of the dipolar bimetallic model. . . . .	30
4.6	Bonding (a) and antibonding (b) plasmon modes of absorption cross-section of the Au@Ag nanorod dimer for different Ag shells $d$ . . . . .	32
6.1	Redshift in the resonant wavelength of a bimetallic nanorod dimer due to binding of a protein molecule . . . . .	41
6.2	Absorption cross-section of the proposed dimer structure to the incident (a) TM and (b) TE polarized light for different Ag shells, $d$ . . . . .	42
6.3	(a) Electric field intensity ( $ E $ ) to the TM polarized light of 710 nm with $d = 1$ nm. (b) Electric field intensity ( $ E $ ) to the TM polarized light of 670 nm with $d = 3$ nm. . . . .	43
6.4	(a) Electric field intensity ( $ E $ ) to the TE polarized light of 663 nm with $d = 1$ nm. (b) Electric field intensity ( $ E $ ) to the TE polarized light of 600 nm with $d = 3$ nm. . . . .	43
6.5	SPR shifts for an APC protein with different shell thickness . . . . .	44
6.6	Absorption cross-section of the proposed dimer structure to the TM polarized light at different lengths, $L$ . . . . .	45
6.7	(a) Electric field intensity ( $ E $ ) to the TM polarized light of 685 nm with $L = 33$ nm. (b) Electric field intensity ( $ E $ ) to the TM polarized light of 818 nm with $L = 44$ nm. . . . .	45
6.8	Absorption cross-section of the proposed dimer structure to the TM polarized light at different widths, $W$ . . . . .	47
6.9	(a) Electric field intensity ( $ E $ ) to the TM polarized light of 868 nm with $W = 7$ nm. (b) Electric field intensity ( $ E $ ) to the TM polarized light of 610 nm with $W = 15$ nm. . . . .	47
6.10	SPR shifts for an APC protein in response to TM incident light with different nanorod lengths (a) and widths (b). . . . .	48
6.11	Absorption cross-section of the proposed dimer structure to the incident (a) TM and (b) TE polarized light at different angles between nanorods. . . . .	49

6.12	Response of the proposed dimer structure to the incident TM and TE polarized light at different angles between nanorods $\theta$ : (a) Electric field intensity ( $ E $ ) to the TM polarized light of 685nm at $\theta = 120^\circ$ . (b) Electric field intensity ( $ E $ ) to the TM polarized light of 685nm at $\theta = 60^\circ$ . (c) Electric field intensity ( $ E $ ) to the TE polarized light of 647nm at $\theta = 120^\circ$ . (d) Electric field intensity ( $ E $ ) to the TE polarized light of 647nm at $\theta = 60^\circ$ . . . . .	50
6.13	SPR shifts for an APC protein in response to TM (a) and TE (b) polarized light with different nanorod positions. . . . .	51
6.14	SPR shifts for an APC protein with different nanorod gap widths . . .	51
6.15	Absorption cross-section of the proposed dimer structure to the TM polarized light at different angles of incidence, $\alpha$ . . . . .	52
6.16	Electric field intensity ( $ E $ ) to the TM polarized light of 685 nm at (a) $\alpha = 0^\circ$ and (b) $\alpha = 60^\circ$ . . . . .	53
6.17	SPR shifts for an APC protein with different incident angles of light ( $\alpha$ ). . . . .	54
6.18	SPR shifts for denatured APC proteins with different chaotropic environment . . . . .	54
6.19	(a) SPR shifts for five bioproteins placed in a fixed gap width of 9 nm. (b) Maximum SPR shifts for the protein samples with optimized gap widths between nanorods. . . . .	56
6.20	SPR shifts for different bioproteins with SiO <sub>2</sub> and TiO <sub>2</sub> substrates . . .	57

# Chapter 1

## Introduction

### 1.1 Nanoplasmonics

When matter is reduced into nanoscale structures, new unique physical properties emerge that are not seen in bulk material. This has fascinated mankind for centuries and forms the basis of nanotechnology, a scientific and technological field that has grown tremendously during the last decades. Nanotechnology deals with materials, systems, and devices on the nanometer length scale (1–100 nanometer) and the concept was first described in 1959 by Richard Feynman in his famous lecture entitled “there’s plenty of room at the bottom” [1]. In his talk he accurately predicted the direction of modern nanotechnology and nanoscience, playing with the idea of miniaturization and atomic engineering. Today, many of the things he anticipated have become reality and we now possess the ability to create and manipulate material at nanoscale dimensions. This has made a significant impact on modern society and the number of applications and products that include nanomaterials increases steadily. Nowadays, nanotechnology is well-established within the manufacturing industry and a respectable scientific field that involves numerous researchers from a wide range of areas including physics, chemistry, biology, medicine, electronics, and engineering.

Nanoplasmonics is a field within nanotechnology that utilizes the unique physical and optical properties of metals [2,3]. These properties are strongly associated with a phenomena known as localized surface plasmon resonance (LSPR) [4–6], which arises when free electrons in metal nanostructures are excited, creating collective electron oscillations confined in the nanostructures. Excitation of localized surface plasmons can be induced by electromagnetic radiation (light) which results in strong scattering and absorption at specific wavelengths which gives metallic nanomaterial distinctive



Figure 1.1: The Lycurgus cup illuminated with ambient lighting (left) and illuminated from inside (right) [7].

colours. The vibrant colours of nanoplasmonic materials have captivated humans for a long time and have been used to decorate glass, ceramics, and mosaics for centuries. One of the most famous artifacts utilizing the optical properties of noble metal nanostructures is the Lycurgus cup (Fig. 1.1), which is a Roman glass cup dated from the fourth century, currently exhibited at the British Museum in London. The cup is of dichroic nature, exhibiting a green jade colour in ambient light and a deep ruby red colour when illuminated from inside. Several analyses have been conducted on the cup in order to understand its optical features [8–10]. These studies have revealed that the cup contains gold-silver (30:70) alloy nanoparticles, 50-100 nm in diameter, embedded in the glass and which absorbs and scatters light at around 515 nm. Although, there are several other examples of glass stained with metal nanoparticles from this era, the Roman glassmakers most certainly produced these objects without knowing that it was actually metal nanoparticles that gave rise to these wonderful colours. Today, nanoplasmonic materials are not primarily used to stain glass anymore but they have, however, found several other applications in many different areas such as optical waveguides [6, 11–13], photovoltaics [14–16], catalysis [17, 18] and finally within chemical and biological sensing [5, 19–27].

## 1.2 Nanoplasmonic Sensing

The excitation of localized surface plasmons in metallic nanostructures using visible light makes nanoplasmonic materials especially attractive for optical sensing applications. When incident light interacts with metal nanostructures, the photons are either absorbed or scattered which is greatly enhanced at the resonance frequency which can be monitored using optical spectroscopy based either on extinction or scattering measurements. When this interaction occurs and light is confined and the energy is converted into a localized surface plasmon, a strong electromagnetic field is created in the direct vicinity of the nanostructures. This highly localized field induced by the LSPR excitation makes metal nanostructures sensitive probes for detecting small, local variations in the surrounding environment. A local change in the refractive index (RI), e.g. due to adsorption of proteins or other biomolecules, can be detected since spectral changes occurs in the light used for LSPR excitation. This forms the basis of nanoplasmonic sensing a simple yet sensitive strategy for detecting biological or chemical interactions. Nanoplasmonic sensing offers real-time, label-free molecular detection and shows a great potential for miniaturization and multiplexing due to the small dimensions of the metal nanoparticles. Refractometric sensing using plasmonic nanostructures have for example been used to detect biomarkers for Alzheimer's disease [28, 29] as well as for cancer [30]. However, most clinically relevant biomarkers are present at very low concentrations, which mean that the sensitivity is a very important aspect to consider when developing bioanalytical sensing devices, in particular for diagnostics. Nanoplasmonic sensors are also employed for a wide number of non-medical applications, such as environmental pollution control, food testing and detection of chemical warfare agents and explosives. In all of these sensing applications, the sensitivity is of critical importance for the overall performance of the sensor system. Methods to improve the sensitivity in LSPR-based sensors have therefore been an area of intense research.

In nanoplasmonic refractometric sensing, the sensitivity for detecting label-free biomolecules close to the metal nanostructures is commonly defined and measured as changes in either the plasmon peak position or intensity due to the local changes in the RI. These measurements are normally performed by monitoring the spectral changes that occurs when plasmonic materials are exposed to solutions with a known RI. The RI sensitivity is highly dependent on the nature of the plasmonic nanoparticles i.e. their size, shape, and metal composition but also on the interaction with other metal

nanoparticles [31,32]. Thus, there are several parameters that influence the sensitivity and by varying the structure, morphology, and surroundings of the plasmonic nanomaterial it is possible to tune the sensitivity and hence, improve the performance of a nanoplasmonic sensing system based on RI detection.

### 1.3 Biomolecule Detection: Present State of the Problem

Recently, biomolecule detection using surface plasmon resonance (SPR) sensors are being extensively studied due to the greater sensing resolution of SPR sensors than that of conventional biosensors, such as piezoelectric and light-addressable potentiometric sensors [33]. Plasmonic sensors based on localized surface plasmon resonance (LSPR) provide a sensitivity of  $\sim 700$  times greater than that in sensors based on other plasmonic resonances for single molecule detection [34]. A number of bio-sensing techniques based on LSPR require fluorophore labels for the samples [35–37]. The labeling procedure increases the cost and complicity of the experimental setup. By contrast, the cost and complicity of the bio-sensing techniques can be reduced significantly by using label-free detection, where bio-molecules are attached to the surface of a noble metal structure, such as gold, silver, and copper [38–40]. When a laser light is exposed to the system, the resonance of absorption changes depending on the presence of the sample biomolecule [19,41]. Although biosensors based on silver (Ag) nanoparticles are approximately twice sensitive than that based on gold (Au) nanoparticles with same geometric properties, they are not preferred due to their easy oxidation and potential toxicity [42]. On the contrary, Au nanoparticles have good biocompatibility and chemical stability. For increased sensitivity, gold core coated by silver shell (Au@Ag) nanospheres have been used for labeled and label-free molecule detection. However, Au@Ag nanorods can provide greater sensitivity than Au@Ag nanospheres due to local field enhancement at the tip. Additionally, significant field enhancement is possible for much sensitive detection if a biomolecule is placed between two metal monomers, i.e., a dimer. Although, proof-of-concept fluorescence enhancement has been demonstrated in a dimer, a detail theoretical analysis including understanding of complex physics is still lacking.



## 1.4 Overview of the Thesis

The objective of our thesis is to investigate the plasmonic properties of Au@Ag nanorod dimers with a view to exploring its sensitivity performance for biomolecule detection. For this purpose, both analytical and numerical analysis have been carried out on the proposed bimetallic system. The dielectric properties of Au@Ag monomer has been explained through a rigorous mathematical model, which in turn explores the absorption spectra of the bimetallic dimers. Optical simulation of these dimers without and with the presence of protein molecules have been carried out by solving the Maxwell's equations in a finite domain time difference (FDTD) method. Many FDTD and finite element simulations are commercially available. For our thesis we have used *Lumerical FDTD solution* for the optical simulation [43].

In chapter 2, a brief overview of LSPR has been given. The Drude-Sommerfeld theory for noble metals has been explained with the derivation of plasma frequency. A rigorous mathematical analysis of LSPR in spherical and spheroidal nanoparticles has been shown through Mie [44] and Gans [45] theory respectively.

In chapter 3, an Au@Ag bimetallic dimer structure has been proposed for the label-free biomolecule detection. A number of protein molecules with significant interest in biochemical and pharmaceutical industries have been chosen as biosamples.

In chapter 4, details of FDTD simulation have been thoroughly discussed. Simulation modeling of noble metals as well as biosamples have been explained with mesh size and boundary conditions.

In chapter 5, an analytical model for the optical properties, e.g. dielectric constant of the Au@Ag nanorod monomer has been developed using the Clausius-Mossotti equation. Using the developed model, the polarizability, electron susceptibility and absorption cross-section of the bimetallic dimers have been calculated.

In chapter 6, the simulated results of the proposed structure have been analyzed without and with the presence of protein molecules. The resonance shifts of the absorption spectra have been calculated, which in turn provides a valid estimation of the molecular sensitivity of the Au@Ag dimer system. Being more sensitive than the traditional Au dimers, the bimetallic structure has been studied with variation of geometric properties as well as physical environment to observe the effects in the absorption spectra due to the presence of a model biosample.

# Chapter 2

## Physics of LSPR

Surface plasmons have attracted the attention of physicists, chemists, biologists and material scientists for widespread use in areas such as electronics, optical sensing, biomedicine, data storage and light generation. Recent developments in nanotechnology have generated new insights about control of various properties of nanomaterials that can support surface plasmons for specific applications. Localized surface plasmon resonance (LSPR) is an optical phenomenon generated by a light wave trapped within conductive nanoparticles (NPs) smaller than wavelength of light. This phenomenon is a result of the interactions between the incident light and surface electrons in a conduction band. This interaction produces coherent localized plasmon oscillation with a resonant frequency that strongly depends on the composition, size, geometry, dielectric environment and particle-particle separation distance of NPs. This chapter gives a rigorous overview of LSPR starting from comparison with SPR and ending with dipolar models of different shapes of NPs.

### 2.1 Bulk Surface and Localized Surface Plasmons

A plasmon is a collective oscillation of the free electrons in a noble metal. It can be described as mechanical oscillations of the electron gas of a metal, the presence of an external electric field causing displacement of the electron gas with respect to the fixed ionic cores. For bulk plasmons, these oscillations occur at the plasma frequency and have energy:

$$E_p = \frac{h}{2\pi} \sqrt{\frac{ne^2}{m\epsilon_0}}, \quad (2.1)$$

where  $\epsilon_0$  is the permittivity of free space,  $n$  is the electron density,  $e$  is the electron charge,  $m$  is the electron mass and  $h$  is the plank constant.

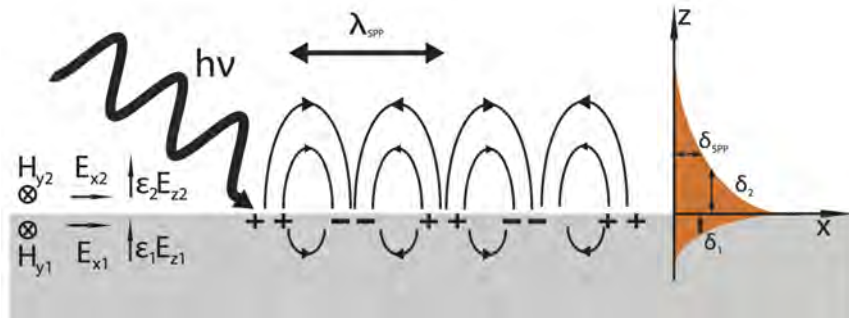


Figure 2.1: Illustration of surface plasmons [46].

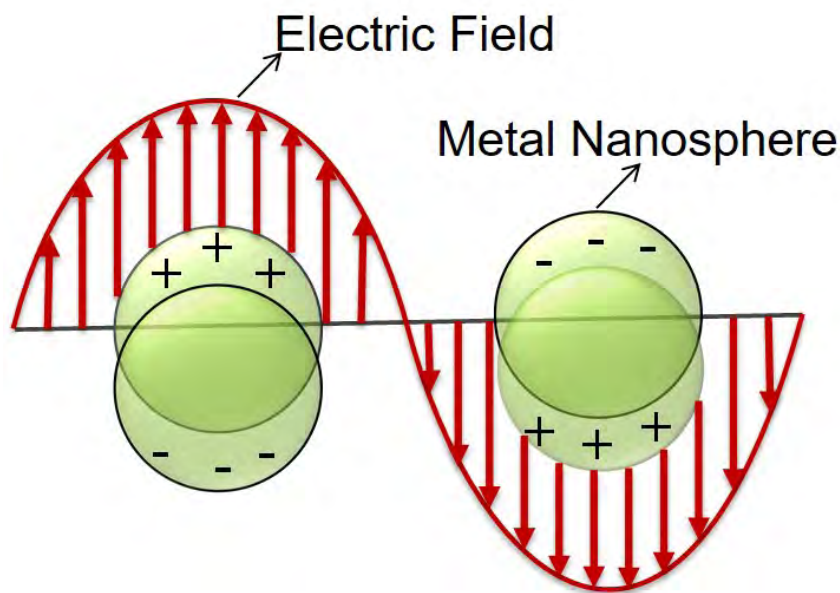


Figure 2.2: Illustration of localized surface plasmons [47].

At the surface of a metal, plasmons take the form of surface plasmon polaritons (SPPs), which has been shown in Fig. 6.19. Surface plasmons are optically excited, and light can be coupled into standing or propagating surface plasmon modes through a grating or a defect in the metal surface. Because it is the oscillating electric field of the incoming plane wave that excites surface plasmons, light with a high angle of

incidence (that is, with wave vector  $k$  nearly parallel to the surface) couples most efficiently.

When a surface plasmon is confined to a particle of a size comparable to the wavelength of light, that is a nanoparticle, the particle's free electrons participate in the collective oscillation, and it is termed a localized surface plasmon (LSP). The concept of LSP has been illustrated in Fig. 2.2. The LSP has two important effects:

- First, electric fields near the particle's surface are greatly enhanced, this enhancement being greatest at the surface and rapidly falling off with distance.
- Second, the particle's optical extinction (absorption and scattering) has a maximum at the plasmon resonant frequency, which occurs at visible wavelengths for noble metal nanoparticles. This extinction peak depends on the refractive index of the surrounding medium and is the basis for the sensing applications.

To understand in depth how this localized surface plasmon resonance (LSPR) arises, we must turn to Drude-Sommerfeld theory.

## 2.2 Overview of Drude-Sommerfeld Theory

To find out the dielectric properties of the nanoparticles, we can start from the Drude-Sommerfeld theory. This model depicts the electrons as a gas of independent quasi-free point-shaped particles that are accelerated by an external electric field and slowed down after a mean free time ( $\tau$ ) through collisions with metal ions (for gold  $\tau_{\text{Au}}=9.3$  fs and silver  $\tau_{\text{Ag}}=30$  fs) [48]. Scattering processes are the reason that the electrons are called quasi-free and not free. The Drude-Sommerfeld model determines the response function or dielectric function  $\epsilon(\omega)$  of a macroscopic metal by calculating the behavior of a single conduction electron and multiplying this behavior by the number of electrons present. This is only valid when assuming the independence of the single electrons, as stated above. The equation of motion for an electron of mass  $m$  and charge  $e$ , in an external electric field  $E = E_0 e^{-i\omega t}$  is given by

$$m \frac{\partial^2 r}{\partial t^2} + m\Gamma \frac{\partial r}{\partial t} = eE_0 e^{-i\omega t}, \quad (2.2)$$

where  $E_0$  is the amplitude of electric field,  $r$  is the displacement of electrons,  $\Gamma$  is

the damping constant and  $\omega$  is the optical frequency. This differential equation only takes into account the effect of the conduction band electrons. In order to incorporate the bound electrons in d-subshells, a linear restoring force,  $m\omega_0^2 r$ , determining the eigen frequency ( $\omega_0$ ) of the oscillating electrons, would have to be added to Eq. (2.2). Solving this equation leads to the dipole moment of a single electron,  $p = er_0$  and the polarization,  $P = np$  with the number of electrons per unit volume  $n$ . The dielectric function,  $\epsilon(\omega) = \epsilon_1(\omega) + i\epsilon_2(\omega)$ , is related to the polarization  $P$  and complex refraction index  $\eta$  via the definition

$$\epsilon = 1 + \frac{P}{\epsilon_0 E}, \quad (2.3)$$

$$\eta + ik = \sqrt{\epsilon}. \quad (2.4)$$

This leads to the dielectric function of a system of  $n$  electrons per unit volume

$$\epsilon(\omega) = 1 - \frac{\omega_p^2}{\omega^2 + i\omega\Gamma} = 1 - \frac{\omega_p^2}{\omega^2 + \Gamma^2} + i \frac{\omega_p^2 \Gamma}{\omega(\omega^2 + \Gamma^2)}, \quad (2.5)$$

where  $\omega_p$  is the plasma frequency and  $\Gamma$  is the damping constant.  $\Gamma$  can be determined from the electron mean free path  $l$  by  $\Gamma = \nu_F/l$ , where  $\nu_F$  is the Fermi velocity. If the damping is much smaller than the frequency, the real ( $\epsilon_1$ ) and imaginary ( $\epsilon_2$ ) parts of the dielectric function can be written as

$$\epsilon_1(\omega) \approx 1 - \frac{\omega_p^2}{\omega^2}, \quad (2.6)$$

$$\epsilon_2(\omega) \approx 1 - \frac{\omega_p^2}{\omega^3} \Gamma. \quad (2.7)$$

This equation shows that for  $\epsilon_1=0$ , the frequency  $\omega$  equals the plasma frequency  $\omega_p$ , which can be defined from Eq. (2.1) as

$$\omega_p = \sqrt{\frac{ne^2}{m^* \epsilon_0}}. \quad (2.8)$$

The dielectric function  $\epsilon(\omega)$  is commonly expressed in terms of the electric susceptibility  $\chi$ . Then Eq. (2.5) becomes

$$\epsilon(\omega) = 1 + \chi(\omega), \quad (2.9)$$

where  $\chi$  is the free-electron Drude-Sommerfeld susceptibility. Electrons in a real metallic lattice are only quasi-free due to the lattice periodicity. The coupling of the free electrons to the ion core is taken into consideration by replacing the electron mass  $m$  with an effective electron mass  $m^*$ , effectively altering  $\omega_p$ .

## 2.3 Mie Theory

In the early 20th century, Gustav Mie developed an analytical solution to Maxwell's equations that describes the scattering and absorption of light by spherical particles [44]. For very small particles, Mie scattering agrees with the more familiar Rayleigh scattering. Finding the scattered fields produced by a plane wave incident on a homogeneous conducting sphere results in the following total scattering, extinction, and absorption cross-sections [49]

$$\sigma_{\text{sca}} = \frac{2\pi}{|k|^2} \sum_{L=1}^{\infty} (2L+1)(|a_L|^2 + |b_L|^2), \quad (2.10)$$

$$\sigma_{\text{ext}} = \frac{2\pi}{|k|^2} \sum_{L=1}^{\infty} (2L+1) [\text{Re}(a_L + b_L)], \quad (2.11)$$

$$\sigma_{\text{abs}} = \sigma_{\text{ext}} - \sigma_{\text{sca}}, \quad (2.12)$$

where  $k$  is the incoming wavevector and  $L$  are integers representing the dipole, quadrupole, and higher multipoles of the scattering. In the above expression,  $a_L$  and  $b_L$  are the following parameters composed of the Riccati-Bessel functions  $\psi_L$  and  $\chi_L$  by

$$a_L = \frac{m\psi_L(mx) \frac{d\psi_L(x)}{dx} - \frac{d\psi_L(mx)}{d(mx)} \psi_L(x)}{m\psi_L(mx) \frac{d\chi_L(x)}{dx} - \frac{d\psi_L(mx)}{d(mx)} \chi_L(x)}, \quad (2.13)$$

$$b_L = \frac{\psi_L(mx) \frac{d\psi_L(x)}{dx} - m \frac{d\psi_L(mx)}{d(mx)} \psi_L(x)}{\psi_L(mx) \frac{d\chi_L(x)}{dx} - m \frac{d\psi_L(mx)}{d(mx)} \chi_L(x)}. \quad (2.14)$$

Here  $m = n/n_m$ , where  $n = n_R + in_I$  is the complex refractive index of the metal, and  $n_m$  is the real refractive index of the surrounding medium. Also  $x = k_m r$ , where  $r$  is the radius of the particle. It is noted that  $k_m = 2\pi/\lambda$  is defined as the wavenumber in the medium rather than the vacuum wavenumber.

To gain insight into LSPR phenomenon, simpler expressions than Eqs. (2.10)–(2.14) are required. If the nanoparticle is assumed to be very small as compared to the wavelength, the Riccati-Bessel functions can be approximated by power series. Following Bohren and Huffman [49] and keeping only terms to order  $x^3$ , Eqs. (2.13) and (2.14) simplify to

$$a_1 \approx -\frac{i2x^3}{3} \frac{m^2 - 1}{m^2 + 2}, \quad (2.15)$$

$$b_1 \approx 0, \quad (2.16)$$

and the higher order  $a_L$  and  $b_L$  are zero (again, only when keeping terms up to  $x_3$ ). To find the real part of  $a_1$  as required in Eq. (2.11),  $m = n_R + in_I/n_m$  needs to be substituted into Eq. (2.15) as

$$a_1 = -\frac{i2x^3}{3} \frac{n_R^2 - n_I^2 + i2n_R n_I - n_m^2}{n_R^2 - n_I^2 + i2n_R n_I + 2n_m^2}. \quad (2.17)$$

Next, switching to the complex metal dielectric function,  $\epsilon = \epsilon_1 + i\epsilon_2$  with the following relations

$$\epsilon_1 = n_R^2 - n_I^2, \quad (2.18)$$

$$\epsilon_2 = 2n_R n_I, \quad (2.19)$$

and switching to medium's dielectric function,  $\epsilon_m = n_m^2$ . These substitutions lead to

$$a_1 = \frac{2x^3}{3} \frac{-i\epsilon_1^2 - i\epsilon_1\epsilon_m + 3\epsilon_2\epsilon_m - i\epsilon_2^2 + i2\epsilon_m^2}{(\epsilon_1 + 2\epsilon_m)^2 + (\epsilon_2)^2}. \quad (2.20)$$

Substituting of Eq. (2.20) into Eq. (2.11) and taking the dipole term yields the widely quoted expression for nanoparticle plasmon resonance as

$$\sigma_{\text{ext}} = \frac{18\pi\epsilon_m^{\frac{3}{2}}V}{\lambda} \frac{\epsilon_2}{(\epsilon_1 + 2\epsilon_m)^2 + (\epsilon_2)^2}, \quad (2.21)$$

where  $V$  is the particle volume. A similar process yields the scattering cross-section

as

$$\sigma_{\text{sca}} = \frac{32\pi^4 \epsilon_m^2 V^2}{\lambda^4} \frac{(\epsilon_1 - \epsilon_m)^2 + (\epsilon_2)^2}{(\epsilon_1 + 2\epsilon_m)^2 + (\epsilon_2)^2}. \quad (2.22)$$

Therefore the absorption cross-section can be found from Eq. (2.12). While these small particle approximations only strictly apply to very small particles, their predictions of dielectric sensitivity are still accurate for larger particles [50].

## 2.4 Gans Theory

Mie theory as formulated above is strictly applicable only to spherical particles. In 1912, Richard Gans generalized Mie's result to spheroidal particles of any aspect ratio in the small particle approximation [45]. He found that the absorption cross-section for a prolate spheroid, analogous to that in Eq. (2.21) above for a sphere, is

$$\sigma_{\text{ext}} = \frac{\omega \epsilon_m^{\frac{3}{2}} V}{3c} \sum_j \frac{(1/P_j^2) \epsilon_2}{\left[ \epsilon_1 + \left( \frac{1-P_j}{P_j} \right) \epsilon_m \right]^2 + [\epsilon_2]^2}. \quad (2.23)$$

Here, the sum over  $j$  considers the three dimensions of the particle,  $P_j$  includes  $P_A$ ,  $P_B$  and  $P_C$ , termed depolarization factors, for each axis of the particle, where  $A > B = C$  for a prolate spheroid. The depolarization factors anisotropically alter the values of  $\epsilon_1$  and  $\epsilon_2$  and the resulting LSPR peak frequencies. Explicitly they are

$$P_A = \frac{1 - e^2}{e^2} \left[ \frac{1}{2e} \ln \left( \frac{1+e}{1-e} \right) - 1 \right], \quad (2.24)$$

$$P_B = P_C = \frac{1 - P_A}{2}, \quad (2.25)$$

where  $e$  is the eccentricity, which includes the particle aspect ratio  $x$  [51, 52] as

$$e = \sqrt{1 - \left( \frac{B}{A} \right)^2} = \sqrt{1 - \left( \frac{1}{x} \right)^2}. \quad (2.26)$$

The absorption spectrum resulting from Eq. (2.23) has two peaks, one corresponding to the transverse plasmon mode and the other corresponding to the longitudinal plasmon mode. Equation (2.23) also provides an intuitive understanding of the effect of aspect ratio on the LSPR peak wavelength. The factor weighting  $\epsilon_m$  which is 2 for spherical particles, is  $[(1 - P_j)/P_j]$  that increases with aspect ratio and can be much greater



than 2. This leads to a red-shift of the plasmon peak with increasing aspect ratio, as well as increased sensitivity to the dielectric constant of the surrounding medium.

## 2.5 Summary

This chapter explains the background theoretical ideas needed to understand LSPR. Drude-Sommerfeld theory provides a detailed study about the dielectric properties of noble metal nanoparticles, including the significance of plasma frequency as well as electron susceptibility. Mie theory demonstrates an analytical modeling of the scattering and absorption of light by spherical particles, whereas Gans theory modifies this modeling in terms of spheroidal particles as well. For nanoparticles beyond the spheres and spheroids, particle shape plays a significant role in determining the LSPR spectrum [53, 54], but one that cannot be found analytically as above, and must be studied numerically. So, the theories discussed in this chapter are the fundamental basis for LSPR generation in any nanoparticles.

# Chapter 3

## Bimetallic Nanorod Dimer Biosensor

### 3.1 Introduction

The last decades have witnessed the ongoing research interests in noble metal nanoparticles (NPs), especially for Au [55–59] and Ag [60–64], mainly due to their interesting optical properties. Specifically, the localized surface plasmonic resonance (LSPR) is derived from the inherent interaction between free electrons of these metal NPs and incident electromagnetic wave [65], which in turn leads to large optical absorption [66], strong Rayleigh scattering [67], and enhanced electronic field coupling [68, 69]. As a consequence, applications of Ag and Au nanostructures have surged, including chemical and biochemical sensing [70–73], medical diagnostics [74], therapeutics [75], waveguides [76], optical devices [77] and surface-enhanced spectroscopies [78–80]. By using different compositions of these two metals, large plasmonic tunability from the visible to near-infrared spectral range can be realized. Specially, bimetallic nanostructures that have prominent plasmonic properties are considered promising candidates for various bio-sensing applications, including labeled and label-free molecule detection. These NPs perform not only a simple combination or enhancement of the properties associated with Au and Ag, but also many interesting and surprising new properties, such as extraordinary plasmonic modes at the interface between the two metals. By changing their components and morphologies, like core-shell architecture, their relevant bio-sensing performances can be successfully modified. The increase of controllable variables leads to inevitable complexity to interpret the interaction mechanism of the bimetallic NPs. Here in, discovering the microstructure nature of their physio-

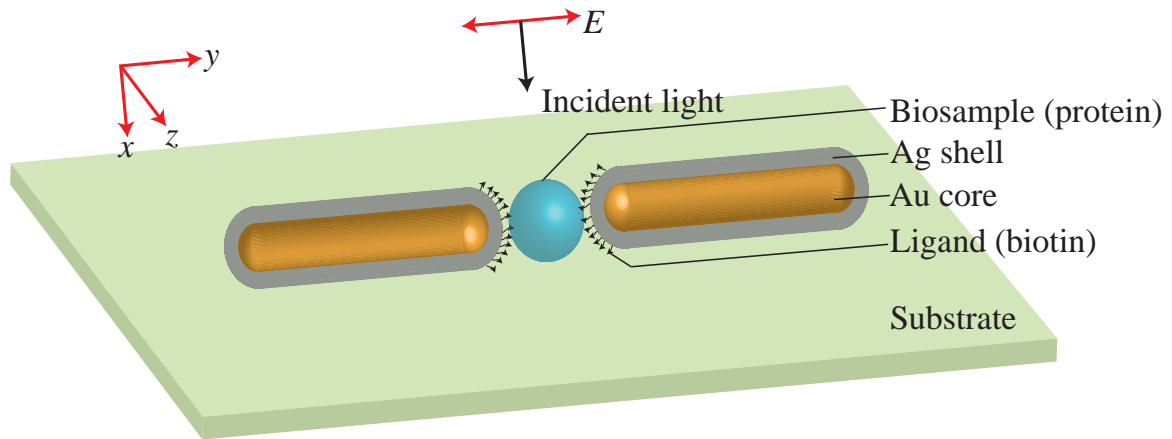


Figure 3.1: Proposed Au@Ag nanorod dimer for biomolecule detection

chemical properties in bimetallic NP system has been attracting great interest of the research scientists.

Recently, a number of studies have been extensively done on Au core coated by Ag shell (Au@Ag) nanospheres to explore its plasmonic properties for bio-sensing application. In addition, dielectric coating, i.e.,  $\text{SiO}_2$  has been added on the bimetallic spheres to improve the sensitivity for biomolecule detection. However, Au@Ag nanorods can provide greater sensitivity than Au@Ag nanospheres due to local field enhancement at the tip region. In addition, significant field enhancement is possible for much sensitive detection if a biomolecule is placed between two nanorod monomers, i.e., a dimer. Although proof of concept fluorescence enhancement has been demonstrated in an Au@Ag dimer, a detailed systematic analysis of the sensitivity performance for different biomolecule detection is still lacking.

## 3.2 Proposed Structure

In Fig. 3.1, we have shown the schematic illustrations of the proposed Au@Ag nanorod dimer. An Au core nanorod has been coated with an Ag shell layer to form the bimetallic nanorod structure with dimensions of  $33 \text{ nm} \times 11 \text{ nm} \times 11 \text{ nm}$ . Due to higher sensitivity of Ag, this structure ensures greater absorption and stronger electric field coupling compared to the Au nanorods. The field coupling of the system has been further enhanced through a longitudinal alignment of two rods with a small gap between the tips, i.e., a bimetallic dimer structure. By varying the core-shell volume of the Au@Ag system, better plasmonic properties can be realized. The whole structure has been placed on a  $\text{SiO}_2$  substrate within a buffer solution to support the bio-sensing

procedure. As we know, the sensing procedure requires the adsorption of biomolecules which involves transport of molecules from the solution to the interface, their binding to the surface usually via hydrophilic, hydrophobic and electrostatic interactions, and their relaxation on the surface via conformational changes. In this work, we have used a number of proteins as biomolecules ranging from 14.3 kDa to 390 kDa to be adsorbed in the gap between the nanorods. From experimental analysis, it has been found that 65% of the protein samples are bound within the gap of a dimer and 35% on the side [81]. Moreover, the enhanced near field intensity at the tip of a particle causes a protein-induced plasma shift 3 to 5 times larger than for a protein binding on the side, halfway the long axis. So, the gap width of the proposed dimer can serve as an optical detector for single protein analysis. Therefore, a 0.5 nm thiolated biotin layer has been coated at the tip of Au@Ag nanorods in the gap region. Such tip functionalized biotinylation is needed to reduce the chemical interface damping of the surface plasmon resonance (SPR) as well. A laser source is placed at normal of the bio-sensor to excite the surface plasmons and hence calculate the absorption cross-section. With a broadband spectrum, significant red-shift would be found at the resonant peaks in presence of protein samples which in turn would execute the sensitivity performance of the proposed bio-sensor.

### 3.3 Protein as a Biomolecule

Single protein detection is a well-researched topic in biochemical and pharmaceutical industries. Proteins detected as biomarkers can benefit a number of scientific and clinical applications such as drug research and environmental monitoring, early disease diagnosis and treatment. A biomarker is a characteristic indicator of a biological phenomenon or state, such as prostate specific antigen (PSA) protein for prostate cancer detection [82]. There are different types of biomarkers ranging from small molecules (i.e., PSA and lysozyme) to large molecules (i.e., fibrinogen and tenascin). In this thesis, we have investigated the molecular detection of five different bioproteins which can be used as potential biomarkers. The samples are:

#### 3.3.1 Lysozyme (Lys)

Lysozyme (Lys), also known as N-acetylmuramide glycanhydrolase, are glycoside hydrolase. These are enzymes that damage bacteria cell walls by catalyzing hydrolysis of

1,4-beta-linkages between N-acetylmuramic acid and N-acetyl-D-glycosamine residues in a polytidoglycan. Large amount of Lys can be found in egg white. Serum lysozyme can be used as a potential biomarker of monocyte/macrophage activity in rheumatoid arthritis.

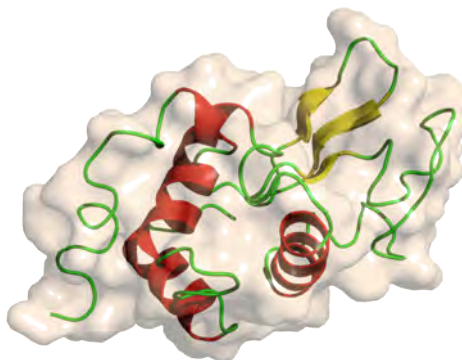


Figure 3.2: Ribbon model structure of lysozyme (Lys) protein

### 3.3.2 Human serum albumin (HSA)

Human serum albumin (HSA) is the version of serum albumin found in human blood. It is the most abundant protein in human blood plasma. It transports hormone, fatty acids and other compounds, buffer pH and maintains oncotic pressure, among other functions. HSA is currently used for investigating human exposure to xenobiotic compounds, including therapeutics and environmental pollutants. A recent study executes that mycotoxin, i.e., satratoxin G (SG) adducts on HSA may serve as biomarkers of exposure to *Stachybotrys chartarum*.



Figure 3.3: Ribbon model structure of human serum albumin (HSA) protein

### 3.3.3 Human $\gamma$ -immunoglobulin (IgG)

Immunoglobulin (IgG), also known as  $\gamma$ -immunoglobulin, is a substance made from human blood plasma. The plasma, processed from donated human blood contains antibodies that protect the body from diseases, such as hepatitis, chickenpox, or measles. Treatments for some cases, i.e., leukemia can cause the body to stop producing its own antibodies, making IgG injection necessary. IgG has been found to be a potential biomarker for acute coronary syndrome (ACS) in adults.



Figure 3.4: Ribbon model structure of human  $\gamma$ -immunoglobulin (IgG) protein

### 3.3.4 Adenomatous polyposis coli (APC)

Adenomatous polyposis coli (APC), also known as deleted in polyposis 2.5 (DP2.5), is a protein in humans encoded by the APC (tumor suppressor) gene. The APC protein is a negative regulator that controls beta-catenin concentrations and interacts with E-cadherin, which are involved in cell adhesion. Mutations in the APC gene may result in colorectal cancer. So, APC has an interesting demand as a biomarker in colon cancer for risk assessment, early detection, prognosis, and surrogate end points.



Figure 3.5: Ribbon model structure of adenomatous polyposis coli (APC) protein

### 3.3.5 Human fibrinogen (Fb)

Fibrinogen (Fb) is a soluble, large glycoprotein in vertebrates that helps in the formation of blood clots. It is one of the 13 coagulation factors responsible for normal blood clotting. Low level of Fb can cause thrombosis leading to serious medical condition, such as heart attack and stroke. Current research reveals its potential functionality as a biomarker for inflammation due to coronary artery disease.

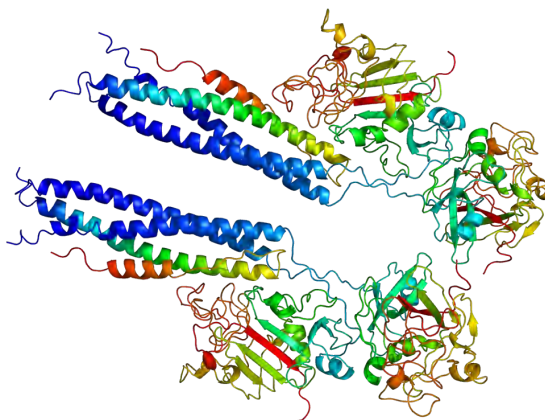


Figure 3.6: Ribbon model structure of human fibrinogen (Fb)) protein

## 3.4 Summary

In this chapter, an Au@Ag bimetallic nanorod dimer has been proposed for better sensitivity performance to label-free molecule detection. Highly sensitive Ag and chemically stable Au are combined in a core-shell structure to enhance the electric field coupling at the tip region. It is expected to produce higher plasmonic shifts in the absorption spectra when a biomolecule is adsorbed in the gap of the dimer. A number of proteins with significant biomarker applications have been selected as biosamples. Proper detection of these molecules through refractive index sensing would lead to an advancement in the research field of nanobiotechnology.

# Chapter 4

## Analytical Modeling of Bimetallic Dimer

### 4.1 Introduction

In many practical cases, the optical properties of the plasmonic-resonant nanostructures can be described by the usual dipolar Rayleigh approximation [49], in which all peculiarities of the light absorption and scattering are determined by the electrostatic polarizability  $\alpha$ . In the case of a homogeneous particle, the polarizability is determined by the particle shape, its dielectric function,  $\epsilon$  and dielectric permittivity of the surrounding environment,  $\epsilon_m$ . Iterative algorithms and analytical models for calculating the polarizability of an arbitrary shaped particle have been developed by researchers for a long time [83,84]. One of the brilliant outcomes of these researches is the electrostatic modeling of the polarizability of spherically symmetric nanoshell structures, which are of great interest for applications to biosensing and immunodiagnostics. As they exhibit extraordinary spectral tunability with size and core-shell aspect ratio, they are currently used in the field of nanobiotechnology. However, the bimetallic core-shell nanorod structures may be considered as a new nanotechnological platform [85], with promising potentialities related to the strong polarized light absorption and tunable longitudinal resonance. It has been found that the bimetallic nanorod systems provide much higher sensitivity for biomolecule detection compared to the spherical nanoshell structures, which is due to their strong electric field coupling at the tip region. The polarizability of these core-shell nanorods exhibit outstanding optical properties of combined noble metal structures, which needs to be elucidated through some theoretical analysis. In this thesis, a simple analytical modeling of electrostatic polarizability



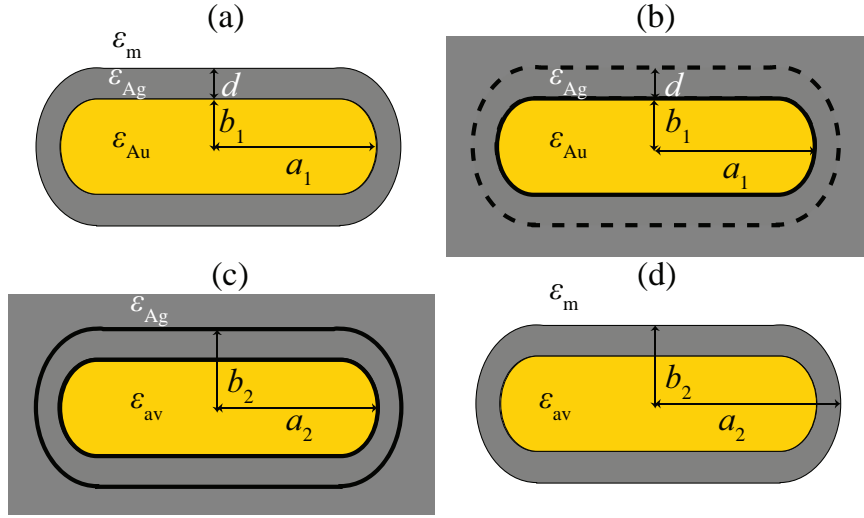


Figure 4.1: The dipole equivalence principle scheme. (a) The initial Au nanorod (semimajor axis-  $a_1$ , semiminor axis-  $b_1$  and dielectric function,  $\epsilon_{\text{Au}}$ ) covered by an outer Ag layer with thickness,  $d$  and dielectric function,  $\epsilon_{\text{Ag}}$ , in a surrounding medium of dielectric function,  $\epsilon_m$ . (b) The initial Au nanorod in the dielectric medium of  $\epsilon_{\text{Ag}}$ , surrounded by an imaginary coating of thickness,  $d$ . (c) An equivalent nanorod with dielectric function of  $\epsilon_{\text{av}}$  in the dielectric medium of  $\epsilon_{\text{Ag}}$ . (d) The equivalent nanorod with semimajor axis-  $a_2$ , semiminor axis-  $b_2$  and dielectric function,  $\epsilon_{\text{av}}$  in the surrounding medium of  $\epsilon_m$ .

has been calculated to explore the optical properties of Au@Ag (Au core with Ag shell) nanorods using the classical Rayleigh [86] and Gans [45] approximation. The principle of dipole equivalency has been used to calculate the equivalent dielectric function ( $\epsilon_{\text{av}}$ ) of silver and gold nanoparticles. The  $\epsilon_{\text{av}}$  has been studied with that of Ag and Au to find out the plasmonic properties of the equivalent system. Finally, the new modeled dielectric function has been used to derive the analytical expressions for polarizability and absorption cross-section of bimetallic nanorod dimers.

## 4.2 Dielectric Function of an Au@Ag Nanorod

The nanorod monomer is treated as a prolate spheroid with a semimajor axis of  $a$  and semiminor axis of  $b$ . The polarizability corresponding to the plasmon mode can be expressed by the Clausius-Mosstti equation as

$$\alpha = \frac{4\pi ab^2}{3} \frac{\epsilon - \epsilon_m}{\epsilon_m + P_L(\epsilon - \epsilon_m)}, \quad (4.1)$$

where  $\epsilon$  is the dielectric function of the nanorod metal,  $\epsilon_m$  is the dielectric function of the surrounding medium, and  $P_L$  is the longitudinal depolarization factor.  $P_L$  can be expressed from Eq. 2.24 as

$$P_L = \frac{1 - e^2}{e^2} \left[ \frac{1}{2e} \ln \left( \frac{1 + e}{1 - e} \right) - 1 \right], \quad (4.2)$$

where  $e$  is the eccentricity of the nanorod defined by  $e = \sqrt{1 - (b/a)^2}$ .

Let us consider a spheroid nanorod of semimajor axis  $a_1$  and semiminor axis  $b_1$  embedded in a homogeneous medium with the dielectric function  $\epsilon_m$ . We are assuming that the nanorod is made of gold with the dielectric function  $\epsilon_{Au}$ . According to Eqs. (4.1) and (4.2), we can express the polarizability  $\alpha_1$  and longitudinal depolarization factor  $P_{L1}$  of the Au nanorod as

$$\alpha_1 = \frac{4\pi a_1 b_1^2}{3} \frac{\epsilon_{Au} - \epsilon_m}{\epsilon_m + P_{L1}(\epsilon_{Au} - \epsilon_m)}, \quad (4.3)$$

$$P_{L1} = \frac{1 - e_1^2}{e_1^2} \left[ \frac{1}{2e_1} \ln \left( \frac{1 + e_1}{1 - e_1} \right) - 1 \right], \quad (4.4)$$

where eccentricity of the Au nanorod  $e_1$  can be defined by  $e_1 = \sqrt{1 - (b_1/a_1)^2}$ .

Let us assume the Au nanorod is surrounded by a dielectric layer of silver with thickness of  $d$  and dielectric function of  $\epsilon_{Ag}$ , just like Fig. 4.1(a). The polarizability of the covered particle can be found from the dipole equivalency principle. To this end, the Au nanorod can be placed in a homogeneous dielectric medium of silver with the permittivity  $\epsilon_{Ag}$  and then surrounded by an imaginary nanorod with semimajor axis  $a_2$  and semiminor axis  $b_2$ , where  $a_2 = a_1 + d$  and  $b_2 = b_1 + d$ . This case has been shown in Fig. 4.1(b). Now the imaginary particle in Fig. 4.1(b) can be replaced by a homogeneous nanorod with same size parameters  $a_2$  and  $b_2$ , and an average dielectric function  $\epsilon_{av}$ , which can be seen in Fig. 4.1(c). The new particle will provide an equivalent dipole moment and polarizability of the bimetallic Au@Ag nanorod monomer. Thus the following equation holds

$$\frac{4\pi a_1 b_1^2}{3} \frac{\epsilon_{Au} - \epsilon_{Ag}}{\epsilon_{Ag} + P_{L1}(\epsilon_{Au} - \epsilon_{Ag})} = \frac{4\pi a_2 b_2^2}{3} \frac{\epsilon_{av} - \epsilon_{Ag}}{\epsilon_{Ag} + P_{L2}(\epsilon_{av} - \epsilon_{Ag})}, \quad (4.5)$$

which simplifies to

$$\frac{a_1 b_1^2}{a_2 b_2^2} \frac{\epsilon_{Au} - \epsilon_{Ag}}{\epsilon_{Ag} + P_{L1}(\epsilon_{Au} - \epsilon_{Ag})} = \frac{\epsilon_{av} - \epsilon_{Ag}}{\epsilon_{Ag} + P_{L2}(\epsilon_{av} - \epsilon_{Ag})}. \quad (4.6)$$

Here  $P_{L2}$  is the longitudinal depolarization factor of the bimetallic Au@Ag nanorod which can be defined as

$$P_{L2} = \frac{1 - e_2^2}{e_2^2} \left[ \frac{1}{2e_2} \ln \left( \frac{1 + e_2}{1 - e_2} \right) - 1 \right], \quad (4.7)$$

where eccentricity of the Au@Ag nanorod  $e_2$  takes the form as  $e_2 = \sqrt{1 - (b_2/a_2)^2}$ .

Equation (4.6) can be considered as the basis for defining the average equivalent polarizability  $\alpha_{av}$ . Now let us assume

$$f = \frac{a_1 b_1^2}{a_2 b_2^2}, \quad (4.8)$$

$$\alpha_s = \frac{\varepsilon_{Au} - \varepsilon_{Ag}}{\varepsilon_{Ag} + P_{L1}(\varepsilon_{Au} - \varepsilon_{Ag})}, \quad (4.9)$$

where  $f$  is the volume fraction of Au core to the equivalent Au@Ag nanorod and  $\alpha_s$  is the polarizability of Au core nanorod in surrounding medium of Ag. So from Eq. 4.6 we can write

$$f\alpha_s = \frac{\varepsilon_{av} - \varepsilon_{Ag}}{\varepsilon_{Ag} + P_{L2}(\varepsilon_{av} - \varepsilon_{Ag})}, \quad (4.10)$$

which reduces to

$$\varepsilon_{av} = \varepsilon_{Ag} \left[ 1 + \frac{f\alpha_s}{1 - f\alpha_s P_{L2}} \right]. \quad (4.11)$$

Equation (4.11) gives the expression for average equivalent dielectric function of the bimetallic nanorod. If the new equivalent nanorod with parameters  $a_2$  and  $b_2$  is placed into the initial dielectric medium  $\varepsilon_m$ , as shown in Fig. 4.1(d), the physical situations in Fig. 4.1(a) and Fig. 4.1(d) will be equivalent. Therefore, the polarizability and dipole moment will also be equivalent and from Fig. 4.1(d) we get

$$\alpha_{av} = \frac{4\pi a_2 b_2^2}{3} \frac{\varepsilon_{av} - \varepsilon_m}{\varepsilon_m + P_{L2}(\varepsilon_{av} - \varepsilon_m)}, \quad (4.12)$$

$$p_{av} = \varepsilon_0 \varepsilon_m \alpha_{av} E, \quad (4.13)$$

where  $\alpha_{av}$  is the equivalent polarizability of Au@Ag nanorod,  $p_{av}$  is the equivalent dipole moment of the Au@Ag nanorod,  $\varepsilon_0$  is the dielectric permittivity of vacuum and  $E$  is the incident electric field on the nanorod.

The absorption cross-section of the bimetallic system will be

$$C_{\text{abs}} = \left( \frac{2\pi}{\lambda} \right) \text{Im}(\alpha_{\text{av}}), \quad (4.14)$$

where  $\lambda$  is the incident wavelength.

In Fig. 4.2, the equivalent dielectric function  $\epsilon_{\text{av}}$  of the Au@Ag system has been analyzed optically for different Ag shell thickness. The real part  $\epsilon_1$  has been shown in Figs. 4.2(a) and 4.2(b), whereas the imaginary part  $\epsilon_2$  has been varied in Figs. 4.2(c) and 4.2(d). Here the bimetallic equivalent nanorod has been fixed at  $a_2 = 16.5$  nm and  $b_2 = 5.5$  nm. The values of  $b_1$  has been varied from 5.5 nm to 0 nm for providing different shell thickness  $d$ . When  $b_1$  is assumed at 5.5 nm,  $d$  turns out to be 0 nm and the equivalent system becomes a bare Au nanorod. On the contrary, when  $b_1$  is reduced to 0 nm,  $d$  is increased to 5.5 nm and the whole Au core nanorod vanishes providing a bare Ag nanostructure. It can be verified from Eq. (4.11) as  $f$  vanishes to 0. For other values of  $b_1$ , such as 4.5 nm, 3.5 nm, and 2.5 nm, the values of  $d$  vary accordingly maintaining the bimetallic structure. The bare Au and Ag system can be analyzed through the real and imaginary parts of  $\epsilon_{\text{Au}}$  and  $\epsilon_{\text{Ag}}$  respectively, which have been referred in the experimental works of Johnson and Christy [87]. Having a look at Fig. 4.2(a), it can be observed that the values of  $\epsilon_1$  encounter a gradual blue-shift towards the corresponding values of  $\epsilon_{\text{Ag}}$  with ascending values of  $d$ . The scenario becomes more clear looking at Fig. 4.2(b), in which zero crossing level has been blue-shifted towards a higher energy of 3.87 eV for larger shell thickness of 3 nm. On the other hand, the interband contribution seen in  $\epsilon_2$  gradually reduces at Fig. 4.2(c), providing more contribution of conduction electrons to the plasma excitation. In Fig. 4.2(d), the reduction in  $\epsilon_2$  becomes more distinct with increasing values of  $d$  from 1 nm to 3 nm. With a view to understanding the plasmonic properties of Au@Ag system, we can investigate the plasma condition of  $\epsilon_{\text{av}}$  by considering the standard plasma dispersion relation in the free electron case which states

$$\epsilon_1(\omega_p) \approx 0, \quad (4.15)$$

$$\epsilon_2(\omega_p) \ll 1, \quad (4.16)$$

where  $\omega_p$  is the plasmon frequency.

In Fig. 4.2(b), the plasmon energies are found at around 3.82 eV–3.9 eV for ascend-

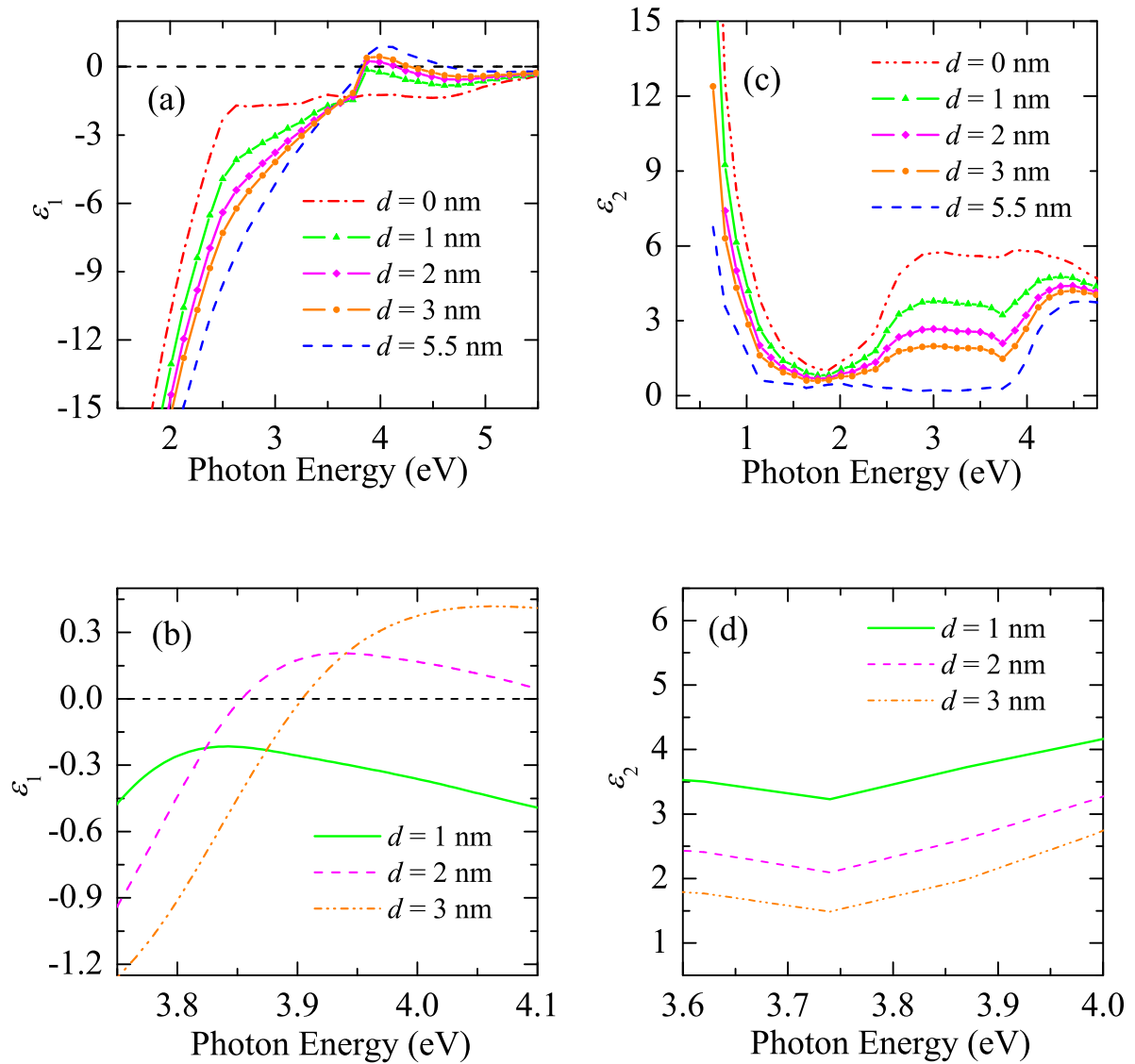


Figure 4.2: Real and imaginary parts of the dielectric function of Au@Ag nanorod system for different Ag shells  $d$ . (a) Extended and (b) zoomed versions of the real parts  $\epsilon_1$  with variation of  $d$ . (c) Extended and (d) zoomed versions of the imaginary parts  $\epsilon_2$  with variation of  $d$ .

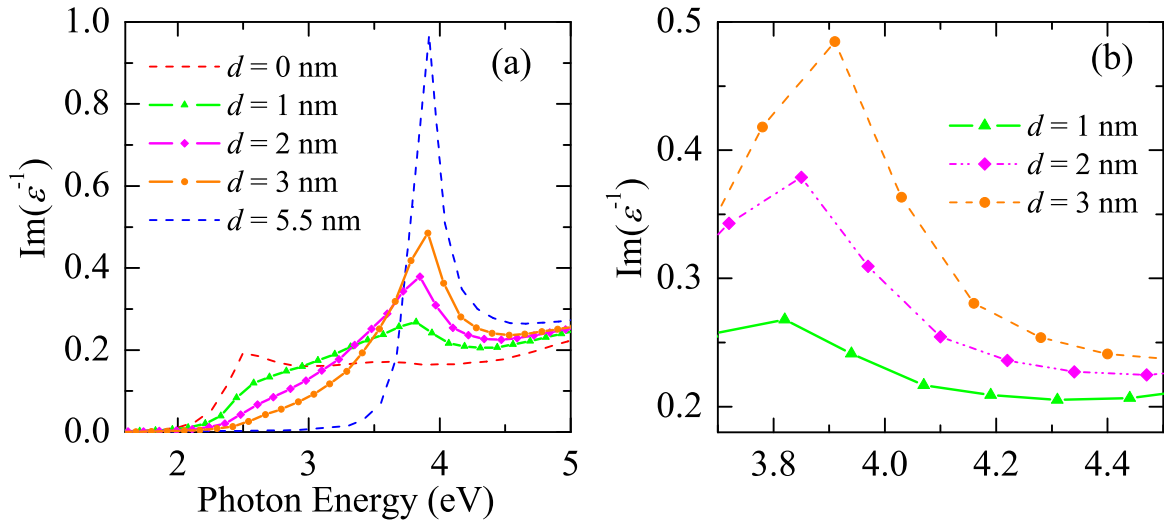


Figure 4.3: (a) Extended and (b) zoomed versions of energy loss function of the bimetallic nanorod system for different Ag shells  $d$ .

ing  $d$  values of 1 nm–3 nm. But the values of  $\epsilon_2$  shown in Fig. 4.2(d), are not less than 1 at these energy levels due to some interband contribution. However, in general, it is not necessary that  $\epsilon_1$  or  $\epsilon_2$  completely vanish near the resonant frequency. In practice, a plasma resonance can be identified by the characteristic maximum in the energy loss function, which is defined as  $\text{Im}(\epsilon^{-1})$ . In Fig. 4.3, the characteristic peak values of the energy loss functions have been varied for different Ag shell widths. Plasmon resonance of the bimetallic system has been found to be greater near the plasmon resonance of Ag, which is accompanied by a gradual blue-shift of plasmon energies in Fig. 4.3(a). The shifts have been clearly identified from 3.81 eV to 3.89 eV in Fig. 4.3(b), when  $d$  has been varied from 1 nm to 3 nm. However, this behavior has already been observed in Fig. 4.2(b). So, it can be concluded that the proposed model in Eq. (4.11) provides a consistent analysis of the dielectric properties of Au@Ag system.

### 4.3 Plasmon Resonance Condition in Bimetallic Nanorod System

From Eq. (4.12), the plasmon resonance is found for the equivalent system when the denominator of average polarizability  $\alpha_{\text{av}}$  is equal to zero (Frohlich condition), that is

$$\epsilon_{\text{av}} = -\epsilon_{\text{m}} \frac{1 - P_{\text{L}2}}{P_{\text{L}2}}. \quad (4.17)$$

From Eqs. (4.11) and (4.17), we can write

$$\varepsilon_{\text{Ag}} \left[ 1 + \frac{f\alpha_s}{1 - f\alpha_s P_{L2}} \right] = -\varepsilon_m \frac{1 - P_{L2}}{P_{L2}}, \quad (4.18)$$

in which applying the value of  $\alpha_s$  we get

$$\frac{\varepsilon_{\text{Au}} - \varepsilon_{\text{Ag}}}{\varepsilon_{\text{Ag}} + P_{L1}(\varepsilon_{\text{Au}} - \varepsilon_{\text{Ag}})} = \frac{\alpha_p}{f}. \quad (4.19)$$

Here parameter  $\alpha_p$  is assumed as

$$\alpha_p = \frac{\varepsilon_m + P_{L2}(\varepsilon_{\text{Ag}} - \varepsilon_m)}{P_{L2}(\varepsilon_{\text{Ag}} - \varepsilon_m)(P_{L2} - 1)}, \quad (4.20)$$

which corresponds to the polarizability of an Ag nanorod with  $\varepsilon_{\text{Ag}}$  embedded in the external medium of  $\varepsilon_m$ .

Now applying componendo-dividendo rule in Eq. (4.19), we get

$$\frac{\varepsilon_{\text{Au}} - \varepsilon_{\text{Ag}} + \varepsilon_{\text{Ag}} + P_{L1}(\varepsilon_{\text{Au}} - \varepsilon_{\text{Ag}})}{P_{L1}(\varepsilon_{\text{Au}} - \varepsilon_{\text{Ag}}) - \varepsilon_{\text{Ag}} - P_{L1}(\varepsilon_{\text{Au}} - \varepsilon_{\text{Ag}})} = \frac{\alpha_p + f}{P_{L1}\alpha_p - f}, \quad (4.21)$$

after simplification which reduces to

$$\varepsilon_{\text{Au}} = -\varepsilon_{\text{Ag}} \left[ \frac{\alpha_p}{P_{L1}\alpha_p - f} - 1 \right]. \quad (4.22)$$

This is the quasi-static relation between core and shell permittivity of the bimetallic nanorod in case of plasmon resonance. When the volume fraction of core is very small ( $f \ll 1$ ), Eq. (4.22) reduces to

$$\varepsilon_{\text{Au}} = -\varepsilon_{\text{Ag}} \left[ \frac{1 - P_{L1}}{P_{L1}} + \frac{f}{\alpha_p P_{L1}^2} \right]. \quad (4.23)$$

In case of thick shell ( $f \approx 0$ ), Eq. (4.23) reduces to the plasmon condition identical to Eq. (4.17) that applies for the Au core of the bimetallic nanorod surrounded by Ag

medium. This provides the validation of Eq. (4.22).

Let us rewrite the resonance condition in Eq. (4.17) in an equivalent form as

$$\varepsilon_{\text{Au}} = -(\varepsilon_{\text{m}} + \chi) \frac{1 - P_{\text{L2}}}{P_{\text{L2}}}, \quad (4.24)$$

where  $\chi$  is the free electron Drude-Sommerfeld susceptibility.

From Eq. (4.22), we can write

$$(\varepsilon_{\text{m}} + \chi) \frac{1 - P_{\text{L2}}}{P_{\text{L2}}} = \varepsilon_{\text{Ag}} \left[ \frac{\alpha_{\text{p}}}{P_{\text{L1}}\alpha_{\text{p}} - f} - 1 \right], \quad (4.25)$$

after simplification which takes the form as

$$\chi = \left( \frac{P_{\text{L2}}}{1 - P_{\text{L2}}} \right) \varepsilon_{\text{Ag}} \left[ \frac{\alpha_{\text{p}}}{P_{\text{L1}}\alpha_{\text{p}} - f} - 1 \right] - \varepsilon_{\text{m}}. \quad (4.26)$$

In case of thick shell ( $f \approx 0$ ), Eq. (4.26) becomes

$$\chi = \left( \frac{P_{\text{L2}}}{1 - P_{\text{L2}}} \right) \varepsilon_{\text{Ag}} \left( \frac{1 - P_{\text{L1}}}{P_{\text{L1}}} \right) - \varepsilon_{\text{m}}. \quad (4.27)$$

In case of thin shell ( $f \approx 1$ ), Eq. (4.26) converts to

$$\chi = - \left( \frac{P_{\text{L2}}}{1 - P_{\text{L2}}} \right) \varepsilon_{\text{Ag}} \left[ 1 + \frac{\alpha_{\text{p}}}{1 - P_{\text{L1}}\alpha_{\text{p}}} \right] - \varepsilon_{\text{m}}. \quad (4.28)$$

Figure 4.4 presents the optical analysis of  $\chi$  for different Ag shells  $d$ . The Ag shells have been varied from 1 nm to 3 nm just the same way done in Figs. 4.2 and 4.3. Here  $\chi$  has been defined as a complex form,  $\chi(\omega) = \chi_1(\omega) + j\chi_2(\omega)$ , in which  $\chi_1$  and  $\chi_2$  present the refractive and absorptive parts of the optical energy respectively. We know that  $\chi$  is practically real for small frequencies when  $d\chi/d\omega$  is positive. It can be realized by positive  $\chi_1$  in Fig. 4.4(a) and almost zero  $\chi_2$  in Fig. 4.4(b) when photon energies are small. This is the realm of classical optics in which the material is mostly refractive. When  $\chi_1$  approaches zero in Fig. 4.4(a), resonance condition occurs due to bound electrons which can be realized by large amount of absorption shown by  $\chi_2$  in Fig. 4.4(b). The resonant energies found in Fig. 4.4(a) are 3.75 eV, 3.79 eV, and



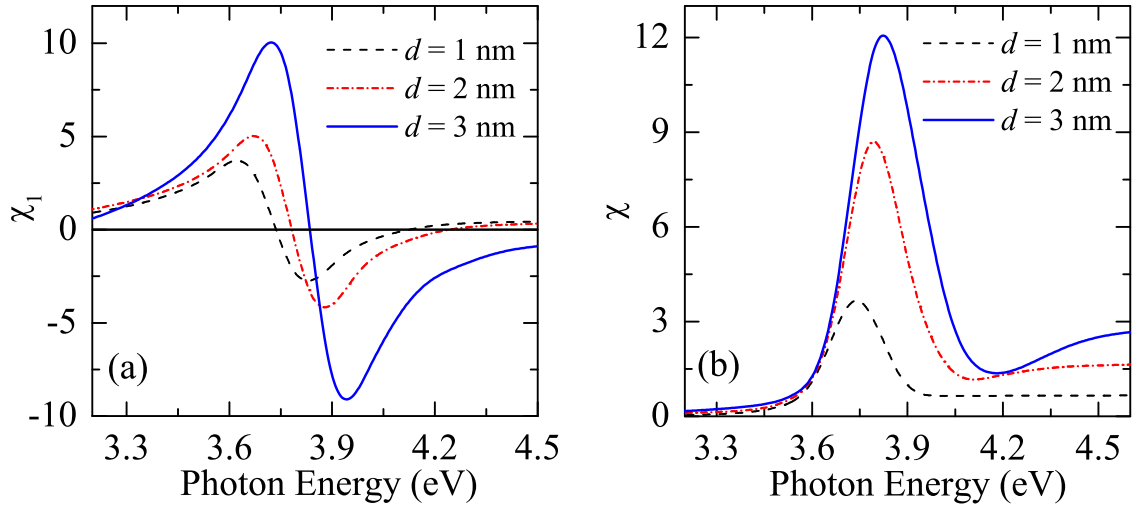


Figure 4.4: Real (a) and imaginary (b) parts of the electron susceptibility of bimetallic nanorod system for different Ag shells  $d$ .

3.82 eV for Ag shells of 1 nm, 2 nm, and 3 nm respectively. All these energies execute maximum absorption in Fig. 4.4(b), providing higher absorption peaks for larger Ag shells. In addition, the resonant energies encounter a gradual blue-shift towards the resonant conditions of bare Ag nanorod system. However, the shift is quite similar to those observed in Figs. 4.2(b) and 4.3(b), where plasmonic properties of Ag becomes prominent with larger shell volume. So, the proposed model of electron susceptibility has been found quite convincing to explain the resonance conditions of Au@Ag nanorod system.

## 4.4 Bimetallic Nanorod Dimer

The polarizability of the equivalent bimetallic nanorod monomer with average permittivity  $\epsilon_{av}$  and surrounded by an external dielectric medium  $\epsilon_m$  can be found from Eq. (4.12) as

$$\alpha_n = \frac{4\pi a_2 b_2^2}{3} \frac{\epsilon_{av} - \epsilon_m}{\epsilon_m + P_{n2}(\epsilon_{av} - \epsilon_m)}, \quad n = L \text{ or } T, \quad (4.29)$$

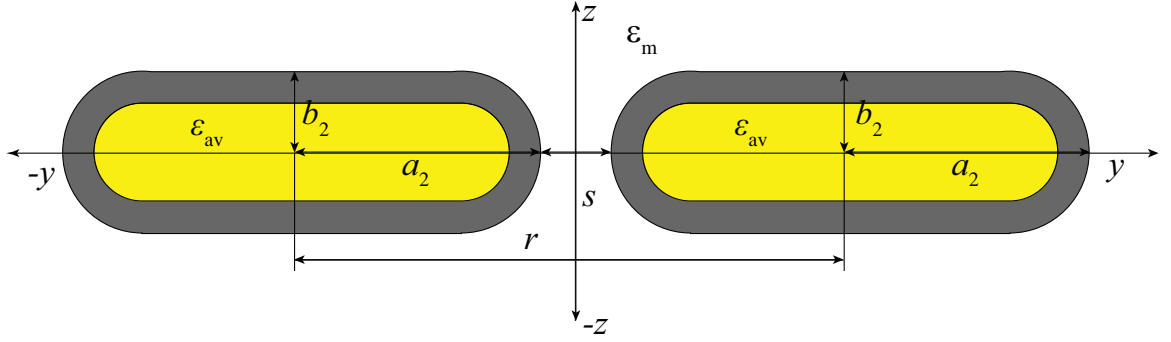


Figure 4.5: Schematic representation of the coordinate system employed in the derivation of the dipolar bimetallic model.

where  $P_{L2}$  and  $P_{T2}$  are the longitudinal and transverse depolarization factors of the Au@Ag nanorod structure. These parameters can be expressed by

$$P_{L2} = \frac{1 - e_2^2}{e_2^2} \left[ \frac{1}{2e_2} \ln \left( \frac{1 + e_2}{1 - e_2} \right) - 1 \right], \quad (4.30)$$

$$P_{T2} = \frac{1 - P_{L2}}{2}, \quad (4.31)$$

$$e_2 = \sqrt{1 - \left( \frac{b_2}{a_2} \right)^2}, \quad (4.32)$$

where  $e_2$  is the eccentricity of the bimetallic system with parameters  $a_2$  and  $b_2$ .

The coordinate system used for the nanorod dimer is shown in Fig. 4.5, where  $y$ -axis is along the longitudinal axis of the dipole system and  $z$ -axis is perpendicular to it. The angle between the two nanorods is  $180^\circ$ . In this coordinate system, the polarizability of the nanorod monomer can be expressed as the combination of longitudinal ( $\alpha_L$ ) and transverse ( $\alpha_T$ ) polarizability along the two axes.

$$\alpha_1 = \alpha_L \hat{\mathbf{j}} + \alpha_T \hat{\mathbf{k}}, \quad (4.33)$$

$$\alpha_2 = \alpha_L \hat{\mathbf{j}} + \alpha_T \hat{\mathbf{k}}, \quad (4.34)$$

where  $\alpha_1$  is the polarizability of nanorod on the left in figure and  $\alpha_2$  is the polarizability of nanorod on the right. As two nanorods are identical, the polarizability should be identical as well. For each nanorod, we have

$$p_i = \varepsilon_0 \varepsilon_m \alpha_i E_i, \quad i = 1 \text{ or } 2, \quad (4.35)$$

where  $\epsilon_0$  is the vacuum permittivity,  $p_i$  is the electric dipole moment of the nanorod  $i$ , and  $E_i$  is the total electric field acting on the nanorod  $i$ .  $E_i$  includes the external field  $E_0$  and the field caused by the electric dipole of the other nanorod. It can be expressed by

$$E_i = E_0 + \gamma \frac{3(p_j \cdot e_{ji})e_{ji} - p_j}{4\pi\epsilon_0\epsilon_m r^3}, j \neq i, \quad (4.36)$$

where  $r$  is the center-to-center distance between the two nanorods,  $e_{ji}$  is the unit vector pointing from the center of the nanorod  $j$  to the center of the nanorod  $i$ , and  $\gamma$  is a coefficient introduced to modify the dipole-dipole interaction. From Fig. 4.5,  $r$  can be defined as

$$r = 2a_2 + s, \quad (4.37)$$

where  $s$  is the gap between two nanorods.

If the external field is considered to be polarized along the  $y$  and  $z$  axis respectively, each of  $p_1$ ,  $p_2$ ,  $E_1$  and  $E_2$  gives two equations for the components along the two axes according to Eqs. (4.35) and (4.36). So, there are totally eight equations for each polarization. We can obtain the relation between the electric dipole moment components and the external field by solving these equations. Summing up the dipole moment components of the two nanorods along each axis yields the dipole moment of the entire dimer system. When the external field is polarized along the  $y$  axis, the bonding plasmon mode is obtained as

$$p_B = p_{1y} + p_{2y}, \quad (4.38)$$

$$p_B = \frac{2\epsilon_0\epsilon_m\alpha_L \left[1 - \frac{\alpha_L\gamma_B}{4\pi r^3}\right]}{1 + \frac{\alpha_L^2\gamma_B^2}{8\pi^2 r^6}} E_{0y}. \quad (4.39)$$

When the external field is polarized along the  $z$ -axis, the antibonding plasmon mode is found as

$$p_A = p_{1z} + p_{2z}, \quad (4.40)$$

$$p_A = \frac{2\epsilon_0\epsilon_m\alpha_T \left[1 + \frac{\alpha_T\gamma_A}{4\pi r^3}\right]}{1 + \frac{\alpha_T^2\gamma_A^2}{8\pi^2 r^6}} E_{0z}. \quad (4.41)$$

In Eqs. (4.39) and (4.41),  $p_B$  and  $p_A$  stand for the electric dipole moments of the bonding and antibonding plasmon modes of the dimer system,  $\gamma_B$  and  $\gamma_A$  are the

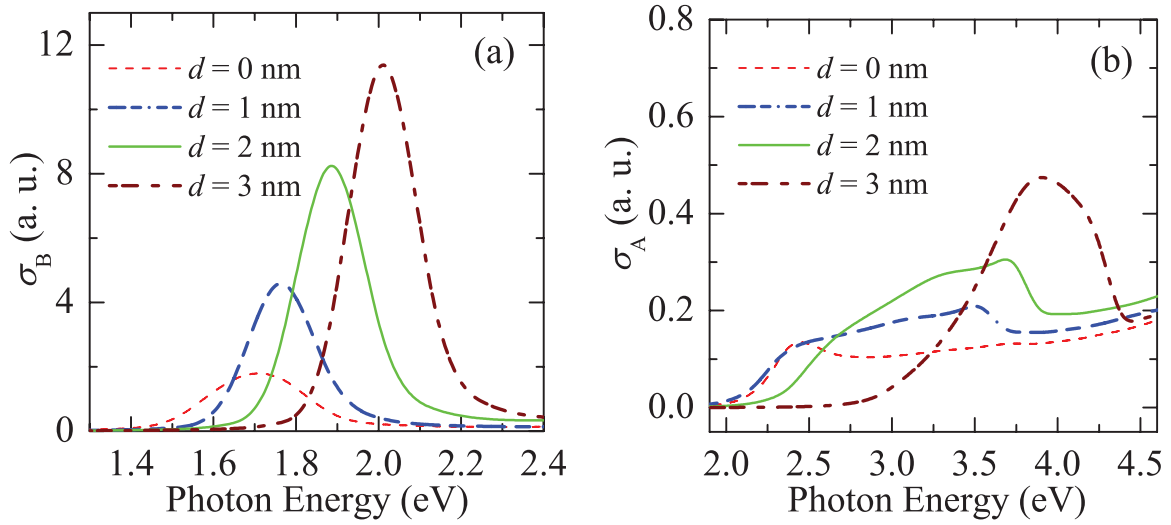


Figure 4.6: Bonding (a) and antibonding (b) plasmon modes of absorption cross-section of the Au@Ag nanorod dimer for different Ag shells  $d$ .

modifying coefficients for bonding and antibonding modes respectively. The values of  $\gamma_B$  and  $\gamma_A$  have been taken as 3.3 and 0.3 respectively [88]. With the help of Eq. (4.14), the absorption cross-section of the bimetallic nanorod dimer can be calculated for bonding and antibonding plasmon modes.

$$\sigma_B = \frac{2\pi}{\lambda} \text{Im} \left[ \frac{2\alpha_L \left[ 1 - \frac{\alpha_L \gamma_B}{4\pi r^3} \right]}{1 + \frac{\alpha_L^2 \gamma_B^2}{8\pi^2 r^6}} \right], \quad (4.42)$$

$$\sigma_A = \frac{2\pi}{\lambda} \text{Im} \left[ \frac{2\alpha_T \left[ 1 + \frac{\alpha_T \gamma_A}{4\pi r^3} \right]}{1 + \frac{\alpha_T^2 \gamma_A^2}{8\pi^2 r^6}} \right], \quad (4.43)$$

where  $\sigma_B$  and  $\sigma_A$  are absorption cross-sections of bonding and antibonding plasmon modes respectively.

Figure 4.6 provides an optical analysis of the derived expression of  $\sigma_B$  and  $\sigma_A$ . Here the absorption of the bimetallic dimer has been varied for different values of  $d$ . The gradual decrease in  $b_1$  from 5.5 nm to 2.5 nm provides a variation of  $d$  from 0 nm to 3 nm, while the value of  $b_2$  is fixed at 5.5 nm. So,  $d = 0$  nm means the system would represent a conventional Au dimer, as already seen in Sec. 4.2. The other values of  $d$  would represent the Au@Ag nanorod dimer at different core-shell ratios. From Fig. 4.6, it is clearly visible that the absorption in bonding mode  $\sigma_B$  is quite large (around 22–25 times) compared to that in antibonding mode  $\sigma_A$ . When  $d$  is varied from 1 nm to 3 nm, absorption of the bimetallic dimer encounters a gradual increase with a larger blueshift in resonant energies. In Fig. 4.6(a), the bonding absorption

of the bimetallic system rises from 4.9 a.u. upto 11.4 a.u. with a resonant energy shift of 1.74 eV to 2.05 eV. This indicates around 2.58–6 times greater absorption than the conventional Au dimer. On the contrary, antibonding modes show very poor absorption for the bimetallic system with resonance at shorter wavelengths, around 310 nm–430 nm shown in Fig. 4.6(b). The  $\sigma_A$  values of the Au dimers are quite comparable to those of Au@Ag system, though the later shows 1.54–3.85 times larger absorption than the former. From this analysis, it is quite evident that the bonding mode would execute superior refractive index sensitivity compared to the antibonding mode. So, the bonding mode would be more effective for applications in biomolecule detection, which proves the consistency of the proposed model of Au@Ag nanorod dimers.

## 4.5 Summary

This chapter provides a theoretical analysis of the optical properties, i.e. dielectric function of the Au@Ag nanorod structure. An analytical expression for the average equivalent dielectric function has been derived to compare the plasmonic behaviors of the bimetallic system with the traditional Au and Ag nanorods. With this proposed expression the plasmon resonance conditions in the bimetallic nanorod system has been explained, which in turn provides a better understanding of the Drude-Sommerfield electron susceptibility. Finally, the polarizability and absorption cross-section of the equivalent Au@Ag nanorod dimers has been analytically modeled for both bonding and antibonding plasmon modes. Absorption profile derived from this analytical model has shown the plasmonic characteristics of the bimetallic dimers with a view to understanding its effectiveness in biomedical applications.

# Chapter 5

## FDTD Simulation

### 5.1 Introduction

The finite difference time domain (FDTD) is an implementation of Maxwell's time-dependent curl equations for solving the temporal variation of electromagnetic waves within a finite space that contains a target of arbitrary shape and has recently become the state-of-the-art method for solving Maxwell's equations for complex geometries. Since FDTD is a direct time and space solution, it offers the user a unique insight into all types of problems in electromagnetics and photonics. Furthermore, FDTD can also be used to obtain the frequency solution by exploiting Fourier transforms; thus, a full range of useful quantities in addition to fields around particles can be calculated, such as the complex Poynting vector and the transmission/reflection of light.

In the FDTD technique, Maxwell's curl equations are discretized by using finite difference approximations in both time and space that are easy to program and are accurate. To achieve high accuracy for realizing the spatial derivatives involved, the algorithm positions the components of the electric and magnetic field about a unit cell of the lattice that constitutes the FDTD computational domain. Each individual cube in the grid is called the Yee cell.

The previous chapter described the plasmonic properties and hence the absorption spectra of the Au@Ag nanorod dimers through a theoretical analysis. This chapter sheds light to the LSPR mechanism in bimetallic dimers by analyzing the proposed structure in Fig. 3.1 using FDTD method. As FDTD is capable of providing the value of fields in any instant and in any position inside the structure, we have been able to study the electric field coupling in Au@Ag dimers with much greater detail. Modeling of the system are presented before the description of results from FDTD and other

simulations.

## 5.2 Material Modeling

Material modeling is one of the most important parts of FDTD simulation work flow. The geometry of a structure is comprised of different materials. Each of the component materials must be properly modeled to account for their dispersive nature. In our thesis, the material modeling is done via experimental values of complex refractive index measured at sampled wavelength values. For intermediate arbitrary wavelength, interpolated values have been used. Silver (Ag) and Gold (Au) exhibit the metal layers in our proposed bimetallic dimer structure. Modeling of the metals is very critical in FDTD analysis as their parameters vary substantially in different data sets. In this work, datas obtained by Johnson and Christy [87] have been used to model Ag and Au. HEPES (10mM N' (2-hydroxyethyl) piperazine-N-ethanesulphonic acid, pH=7.4) has been considered as the buffer medium, which is currently used in extensive biosensor research. For our simulation, the refractive index (RI) of HEPES buffer has been chosen as 1.332 [89]. To model the glass substrate we have taken frequency dependent RI values of SiO<sub>2</sub>, which has been varied from hydrophilic TiO<sub>2</sub> to hydrophobic Teflon-AF to show the substrate effects.

## 5.3 Biomolecule Modeling

Modeling of biomolecules is yet another important factor of FDTD simulation. The biosensing performance of the proposed structure largely depends on how the protein samples are modeled. It is required to model the bioproteins according to their original sizes and shapes, otherwise practical results can not be predicted from the FDTD simulation. In this study, we have taken protein samples with significant differences in their tertiary sizes ranging from 14.3 kDa to 390 kDa. The adsorption of chicken egg white lysozyme (Lys), human serum albumin (HSA), human  $\gamma$ -immunoglobulin (IgG), adenomatous polyposis coli (APC) and human fibrinogen (Fb) have been modeled on glass substrate in between the gap of Au@Ag dimer. Characteristic differences of these proteins have been highlighted through shapes and refractive index (RI), which have been referred from the experimental analysis [89,90]. The sizes, shapes and RI values of these modeled biosamples are shown in the following table:

Table 5.1: Characteristic differences of the simulated protein models

Protein	Dimension (nm)	Mass (kDa)	Refractive Index
Lys	$1.9 \times 1.9 \times 1.9$	14.3	1.495
HSA	$8 \times 7 \times 4$	66.4	1.45
IgG	$4 \times 3.6 \times 3$	148	1.42
APC	$4.8 \times 4.5 \times 4.3$	275	1.46
Fb	$46 \times 3 \times 6$	390	1.39

A 0.5 nm biotin layer has been added around the tips of the nanorods in the gap region of dimer. The RI value of this biotin has been considered as 1.45, being referred in [34]. With the proposed structure incident at transverse magnetic (TM) and transverse electric (TE) polarized light, the SPR shifts for these bioproteins have been calculated to find out the molecular sensitivity of the proposed bimetallic dimers.

## 5.4 Mesh Independence Test

The validation test of the FDTD simulation are done by looking for consistency of the simulation results with the experimental and theoretically predicted values. The matched results validate the simulation procedure. To maintain the accuracy and stability of the FDTD calculations, mesh independence test has been performed by first finding the threshold mesh size. The threshold mesh size is the largest grid size to accurately model the prescribed system without being computationally prohibitive. Traditionally, it is obtained in an iterative fashion (convergence testing). By starting from a very small mesh size, it has been increased until the simulation gives diverging results. The lowest mesh size which gives diverging results are the threshold mesh size. We have chosen a spatial mesh size of 0.5 nm, as because it is smaller than the threshold mesh size (0.75 nm) and the halving of this mesh size, although increases the simulation time considerably, yields same results. FDTD algorithm requires the time increment have a specific bound relative to the spatial discretization (grid/mesh size) to ensure the stability of the time-stepping algorithm. In our implementation of FDTD, the time step and hence the total time of simulation has been determined by the values of the spatial grid to ensure numerical stability. With considering our sensor size and mesh grid, we have chosen 300 fs for total simulation time with a minimum time step of 0.00095 fs.



## 5.5 Boundary Conditions

Depending on the purpose of the optical simulation some kind of boundary conditions must be imposed. Boundary conditions are nothing more than mathematical description that defines how field quantities should behave as they reach the edge of the simulation region. For simulation purpose, mainly two sets of boundary condition were used. One is perfectly matched layer (PML) and the other is periodic boundary condition.

### 5.5.1 Perfectly Matched Layers

Perfectly matched layer (PML) defines the boundary condition that ensures that outgoing radiations that reach the edge of the simulation boundary will die out at the boundary without reflecting back into the simulation region to interfere with the field inside. An ideal PML boundary will absorb all of the electromagnetic field incident on it. However, this does not happen in real PML condition. Depending on the number of layers, a real PML can only approximate an ideal PML boundary with different accuracy. While the absorption is maximum in case of normal incidence, oblique incidence can result in significant reflection back into simulation region. So number of layers must be chosen carefully in a the direction of interest to simulate the practical scenario as accurately as possible. In our simulation we have taken 12 layers to provide consistency with the experimental results. Also this boundary condition works best if the structure is extended through the simulation boundary. PML boundary is used to simulate and study the behavior of an isolated structure. If a structure is surrounded by a simulation region with PML boundary condition imposed on every side, it can be assumed to be isolated. The only excitation source will be the source placed within the boundary. The electromagnetic field profile observed after simulation will be only due to the perturbation of that structure alone.

### 5.5.2 Periodic

Periodic boundary condition is mainly used with broadband wave source. Unlike PML, field does not exactly die out at the edge of the simulation region. Rather it assumes that similar structure continues in that direction. FDTD simulator then takes into account of presence of similar structure in the direction and calculates the field profile accordingly. It is possible to impose different boundary conditions on different

directions.

For the simulation of Au@Ag nanorod dimer biosensor a mix of both of these two conditions is used. A PML is imposed on the direction of incident wave ( $x$ -axis for this case) and on the longitudinal axis ( $y$ -axis). Besides, periodic condition is used on the transverse axis ( $z$ -axis) along which the structure is symmetric. With this boundary conditions it is easier to calculate the absorption and electric field coupling in the dimer sensor at a much smaller simulation time.

## 5.6 Optical Sources

Optical source modeling is very important for proper optical simulation of a given structure. In this work, we have used Total Field Scattered Field source (TFSF source) which is particularly used for understanding the behavior of scattering and absorption from small particle. It is also convenient to properly evaluate the electric field enhancement at the edges of nanorod structure. A TFSF source is modeled in such a way that it splits the simulation region in two different regions.

- Total field region: It contains the total field of (the summation of absorbed and scattered field).
- Scattered field region: It only contains the scattered field.

Within the boundary of the source it is a plane wave that propagates with a wavevector normal to its surface of incidence. At the edge of the boundary the absorbed field is subtracted from the total field leaving only the scattering field to propagate outside. When it acts as a plane wave it can be defined to have a fixed polarization. Depending on the angle of polarization it will give TE (for angle  $90^\circ$ ) or TM (for angle  $0^\circ$ ) wave propagation in 3D simulation.

## 5.7 Power Absorption

Spatial power absorption in the structure was calculated using the formula

$$P_{\text{abs}} = \frac{1}{2} \times \omega \times \text{Imag}(\epsilon) \times |E|^2. \quad (5.1)$$

Here,  $\epsilon$  is the permittivity of the material at the point at which the absorption is being calculated,  $\omega$  is the frequency of the incident light, and  $E$  is the electric field

intensity. The power absorption is then integrated along spatial co-ordinates in order to find the total absorption with respect to frequency/wavelength in the structure. The calculation of total absorption spectrum is very significant as it provides the resonance shifts and hence the sensitivity performance for different protein samples.

## 5.8 Summary

FDTD simulation is a general computational electromagnetic tool, that can simulate very general structures. Interest in FDTD Maxwell's equations solvers has increased nearly exponentially over the past 20 years. Increasingly, engineers and scientists in non-traditional electromagnetics-related areas such as photonics and nanotechnology have become aware of the power of FDTD techniques. Yet to the best of our knowledge, we have simulated the Au@Ag nanorod dimer structure for exploring its bio-sensitivity by complete 3D FDTD method for the first time. FDTD has lead us to results that are theoretically and experimentally expected. Simulation of much complicated photonics structures for biomolecule detection will be possible with FDTD method.

# Chapter 6

## Simulation and Result Analysis

### 6.1 Introduction

Theoretical investigations of LSPR are critical to understand the light dynamics in sub-wavelength sample and metal layers, and to predict the experimental observations. Till date, in theoretical investigations, power absorption and scattering spectrum have been extensively studied to find out the characteristics of LSPR biosensors. Moreover, shifts in resonant wavelengths for different biomolecules have also been calculated to find out the sensitivity of metal nanoparticles. In this thesis, we have considered absorption cross-section rather than scattering as because the efficiency of absorption dominates over the scattering when particle size is very small (much less than wavelength). Different parameters (i.e., core-shell ratio, aspect ratio, gap width) of the Au@Ag nanorods have been varied to observe the effects on the absorption spectrum as well as electric field coupling at the tip region. The optical source has been placed at different incident angles (i.e.,  $30^\circ$ ,  $45^\circ$ ,  $60^\circ$ ) rather than at normal to find out the differences at the absorption characteristics. The nanorods have also been positioned at various inter-rod angles (i.e.,  $150^\circ$ ,  $120^\circ$ ,  $90^\circ$ ,  $60^\circ$ ) to study the effects on the SPR properties. With a view to investigating the molecular sensitivity, a number of proteins has been used as biosamples. Peak shifts at resonant wavelengths have been calculated for these biomolecules considering of various parameters, such as core-shell ratio of nanorods, substrate, physical environment etc. A general scenario of this SPR shift has been shown in Fig. 6.1 in terms of absorption cross-section ( $\sigma$ ) of the Au@Ag nanorod dimers. As the simulation structure as well as surrounding environment executes a proper scenerio of the experimental setup, it is expected that the SPR shifts calculated here would provide a clear picture about sensitivity of the bimetallic system.

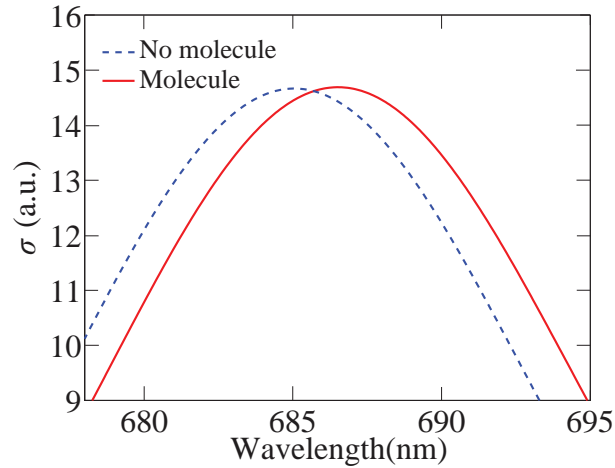


Figure 6.1: Redshift in the resonant wavelength of a bimetallic nanorod dimer due to binding of a protein molecule

## 6.2 Physical Parameters of Nanorod Monomers

### 6.2.1 Core-Shell Ratio

The core-shell fractional volume is the most important and unique parameter that can be varied to improve the sensitivity of any bimetallic biosensor. Colloidal metal nanoparticles, specially Au@Ag nanospheres have already been studied with different core-shell ratios to explore its plasmonic functionality and application in biochemical and pharmaceutical industries. In this section, we have investigated the plasmonic properties of Au@Ag nanorod dimers with respect to different core-shell volumes. We have varied the volume fraction of Au core in terms of  $b_1$ . Just like Sec. 4.2, the equivalent nanorod size has been fixed with  $a_2 = 16.5$  nm and  $b_2 = 5.5$  nm. Gradual decrease in  $b_1$  from 4.5 nm to 2.5 nm has resulted in an increase in  $d$  from 1 nm to 3 nm.

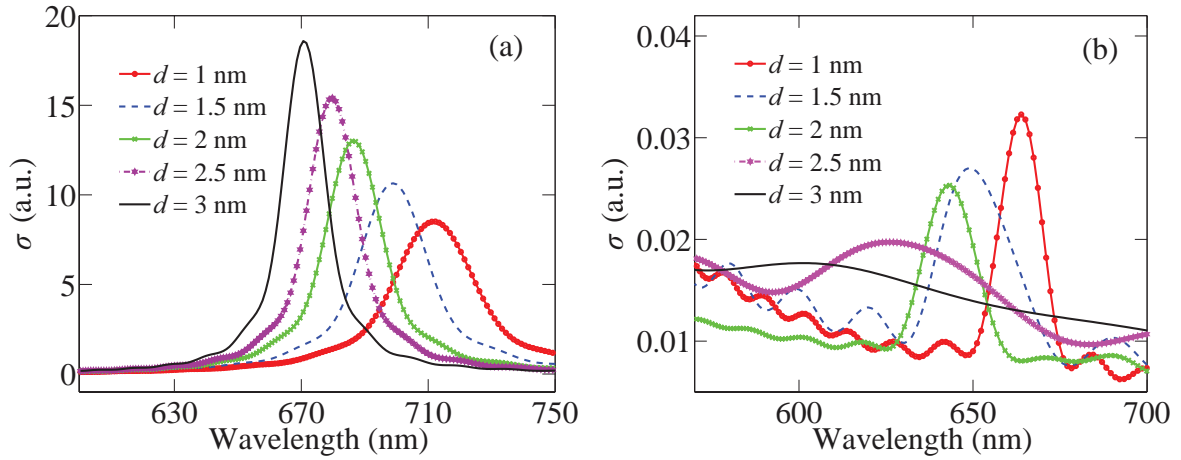


Figure 6.2: Absorption cross-section of the proposed dimer structure to the incident (a) TM and (b) TE polarized light for different Ag shells,  $d$

Figure 6.2 presents the absorption spectrum of Au@Ag dimers to the incident transverse magnetic (TM) and transverse electric (TE) polarized light for different core-shell volumes. Here TM polarization produces the bonding plasmon mode and hence increases the optical absorption with larger Ag shell thickness. This phenomenon can be realized by gradual increase in absorption peaks from 8.3 a.u. to 19.2 a.u. with ascending values of  $d$ , as shown in Fig. 6.2(a). Compared to TM, TE polarized light causes very negligible absorption in the dimer system due to the antibonding plasmon mode. Progressive increase in  $d$  results in a reduction in the absorption peaks from 0.032 a.u. to 0.018 a.u., which can be observed in Fig. 6.2(b). In both polarizations, the absorption spectrum executes a gradual blue-shift with larger values of Ag shells. This behavior has already been seen at the theoretical modeling of the bimetallic dimer in Fig. 4.6. However, the above analysis provides a clear justification of the analytical model proposed in Chap. 4.

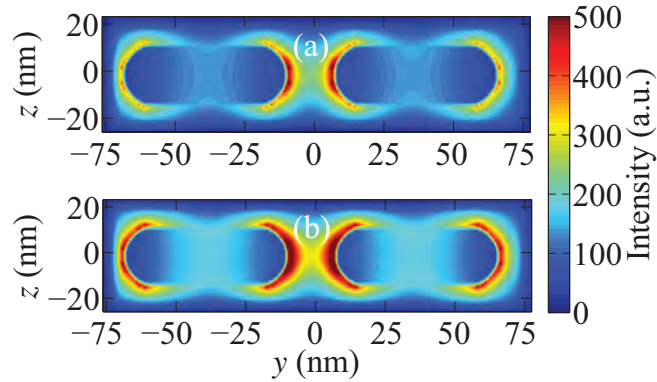


Figure 6.3: (a) Electric field intensity ( $|E|$ ) to the TM polarized light of 710 nm with  $d = 1$  nm. (b) Electric field intensity ( $|E|$ ) to the TM polarized light of 670 nm with  $d = 3$  nm.

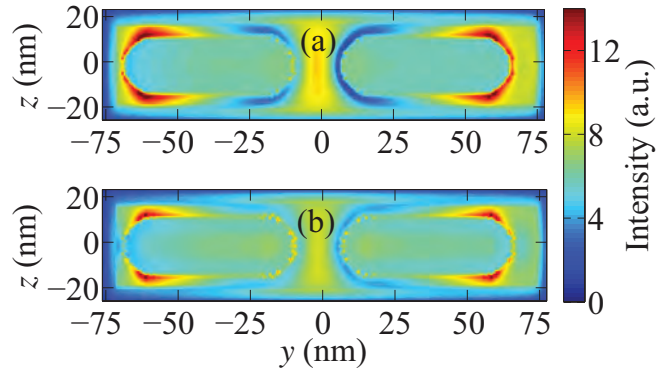


Figure 6.4: (a) Electric field intensity ( $|E|$ ) to the TE polarized light of 663 nm with  $d = 1$  nm. (b) Electric field intensity ( $|E|$ ) to the TE polarized light of 600 nm with  $d = 3$  nm.

From this discussion it is quite obvious that the TE polarization in bimetallic system is not suitable at all for biomolecule detection. To have a more clearer view, we have studied the electric field intensity ( $|E|$ ) of the Au@Ag dimers for TM and TE incidence at different resonant wavelengths, shown in Fig. 6.3 and Fig. 6.4 respectively. Here we have used two bimetallic dimer systems with different core-shell fractions. In Figs. 6.3(a) and 6.3(b), we present the  $|E|$  profile at resonant wavelengths of 710 nm and 670 nm, which correspond to the dimer shell of 1 nm and 3 nm respectively. Similarly in Figs. 6.4(a) and 6.4(b), we exhibit the field coupling at resonant wavelengths of 663 nm and 600 nm respectively, which correspond to same order of shells

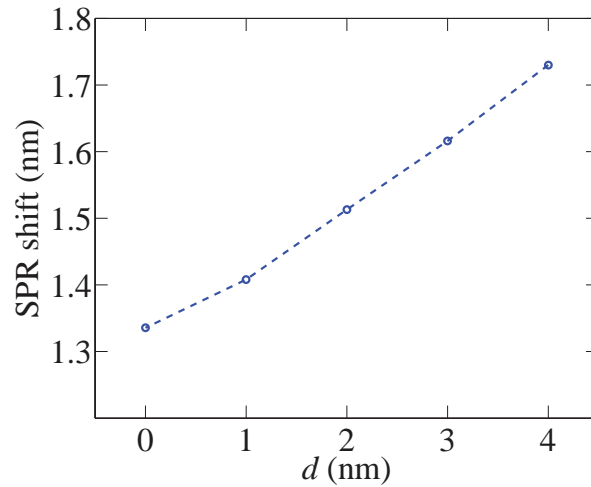


Figure 6.5: SPR shifts for an APC protein with different shell thickness

as Fig. 6.3. The TM field profile in Fig. 6.3 shows greater enhancement at 670 nm compared to 710 nm, whereas TE field in Fig. 6.4 exhibits weaker coupling at 600 nm compared to 663 nm. Both these figures clearly suggest for stronger TM but weaker TE field intensity for larger shell thickness. This phenomenon is quite consistent with the absorption spectrum observed in Fig. 6.2. So, we can clearly understand that the proposed Au@Ag dimer structure is more suited to TM polarization rather than TE for single molecule detection.

With a view to exploring the bio-sensitivity we have investigated the SPR shifts for an APC protein model with different core-shell ratios of the proposed structure. Fig. 6.5 displays the shift dependence in the absorption spectra for TM polarized light. We have varied the core-shell ratio with different values of  $d$  ranging from 0 nm to 4 nm. From previous discussion we already know that 0 nm of shell would result in a conventional Au dimer structure. So SPR shift for this case will simply exhibit the sensitivity of bare Au dimers. When  $d$  is varied in the ascending order, resonance shifts due to APC biosample rises from 1.3356 nm to 1.73 nm, executing a 6%–30% higher sensitivity compared to the popular Au structure. The betterment in sensitivity can be verified with other protein samples as well. So, from the above analysis we can conclude that higher shell fraction of Ag provides stronger field coupling and hence larger resonance shifts in the proposed dimer which makes it a more efficient and reliable biosensor for label-free molecule detection.



### 6.2.2 Aspect Ratio

With a view to investigating the plasmonic sensitivity of metal nanorods, the most common factor that has been extensively studied is the aspect ratio. Variation of lengths and widths provide more feasibility to investigate plasmon coupling than any other parameter. In this section, we have discussed the plasmonic dependence of the proposed dimer system on the aspect ratio  $R$  of bimetallic nanorods. For this analysis, we have maintained a fixed core volume fraction of 0.909 and varied the physical parameters of nanorod accordingly. As we know  $R$  is simply defined by the fraction of length  $L$  and width  $W$ , we have studied the effects of different  $R$  through varying  $L$  and  $W$  systematically.

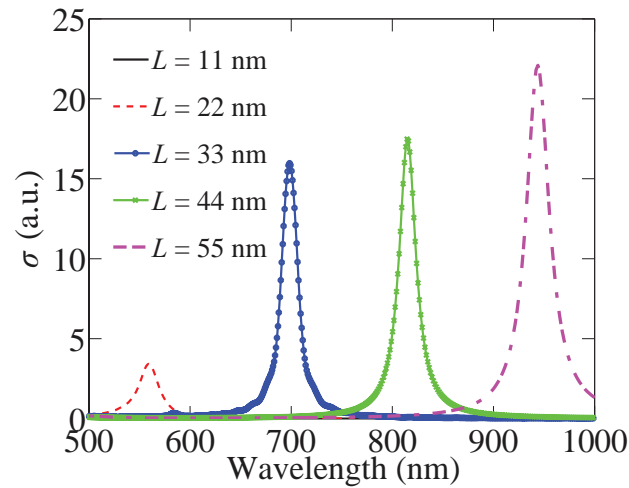


Figure 6.6: Absorption cross-section of the proposed dimer structure to the TM polarized light at different lengths,  $L$ .

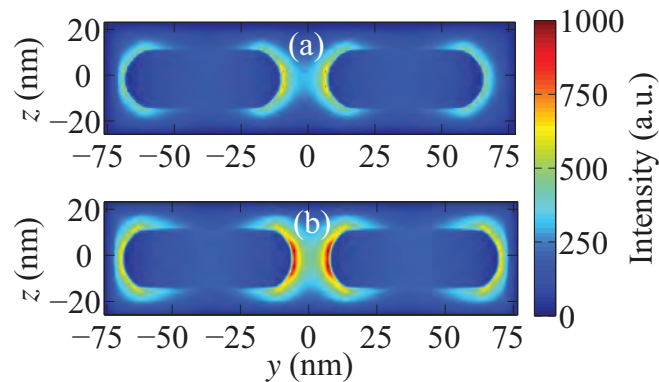


Figure 6.7: (a) Electric field intensity ( $|E|$ ) to the TM polarized light of 685 nm with  $L = 33$  nm. (b) Electric field intensity ( $|E|$ ) to the TM polarized light of 818 nm with  $L = 44$  nm.

### Variation of length

Figures 6.6 and 6.7 show the response of the proposed structure to the incident TM polarized light at different lengths of nanorods. TE incidence has been found to be insignificant in longitudinal modes of dimers, so it has been discarded. In Fig. 6.6 we have analyzed the absorption cross-section for five different lengths  $L$ : 11 nm, 22 nm, 33 nm, 44 nm and 55 nm. The width has been fixed at 11 nm, which results in a fixed  $b_2$  of 5.5 nm. The values of  $a_2$  have been varied to vary the length. We have started our analysis from simple nanosphere ( $R = 1$ ) to the elongated rod structure ( $R = 5$ ). Having a look at Fig. 6.6, we can see that the absorption in the nanosphere ( $L = 11$  nm) is very much small compared to other structures. Moreover the absorption profile becomes larger with ascending values of  $L$ , that means higher values of  $R$ . The concept gets verified with a detailed study of  $|E|$  profile for different values of length. We present the field intensity in Figs. 6.7(a) and 6.7(b) at two resonant wavelengths, 685 nm and 818 nm, which corresponds to lengths of 33 nm and 44 nm respectively. The field profiles clearly indicate stronger coupling at 818 nm compared to 685 nm, which corresponds to greater sensitivity for larger length and hence larger aspect ratio.

### Variation of width

To show the variation of width we have taken a bimetallic nanorod of 33 nm long. So  $a_2$  has been fixed at 16.5 nm while  $b_2$  has been varied to vary the width. In Fig. 6.8 we have shown the absorption profile for five different width values  $W$ : 7 nm, 9 nm, 11 nm, 13 nm, and 15 nm. Highest absorption peak is found for 7 nm, corresponding to the aspect ratio  $R$  of 4.7. The peak gradually decreases from 15.7 a.u. to 10.1 a.u. for ascending values of  $W$ , referring to weaker coupling for wider nanorods. This idea can be established with a detailed study of  $|E|$  profile for different width values. Figures 6.9(a) and 6.9(b) exhibit field coupling at two resonant wavelengths, 868 nm and 610 nm, which correspond to nanorod widths of 7 nm and 15 nm respectively. In response to these figures it can be clearly seen that the intensity has been drastically decreased at 610 nm compared to 868 nm. The decrease in  $E$  profile corresponds to a decrease in  $R$ . So, after a detailed study it is quite obvious that the plasmon coupling is stronger for higher values of  $R$ , i.e., lower values of  $W$ , which provides a verification of the previous discussion.

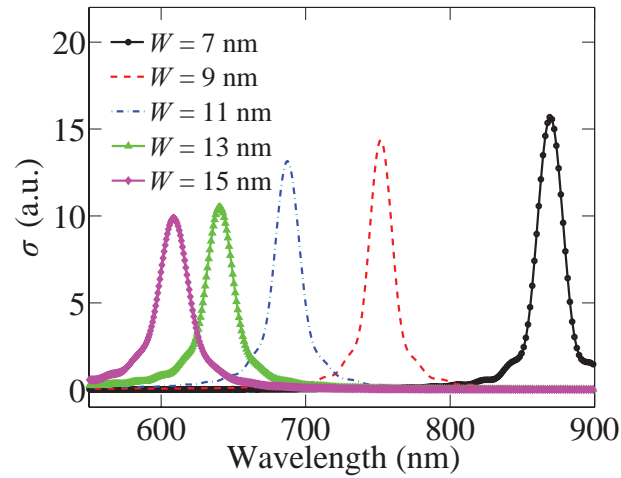


Figure 6.8: Absorption cross-section of the proposed dimer structure to the TM polarized light at different widths,  $W$ .

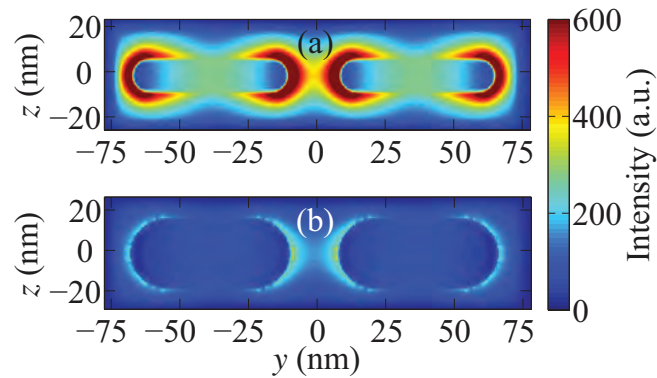


Figure 6.9: (a) Electric field intensity ( $|E|$ ) to the TM polarized light of 868 nm with  $W = 7$  nm. (b) Electric field intensity ( $|E|$ ) to the TM polarized light of 610 nm with  $W = 15$  nm.

With a view to investigating the effects of  $R$  on bio-sensitivity of the bimetallic system, we have analyzed the modeled dependence of SPR shifts for an APC protein on different lengths and widths, as shown in Fig. 6.10. The gradual increase in peak shifts from 0.1 nm to 1.94 nm has clearly verified the increasing effect of  $R$  in Fig. 6.10(a). By contrast, progressive increase in widths has led to a decrease in shift values from 2.28 nm to 1 nm, which in turn proves the decreasing effect of  $R$  in Fig. 6.10(b). However, both figures have provided clear evidence for variation of  $R$  which can be further implemented for performance improvement of Au@Ag biosensors.

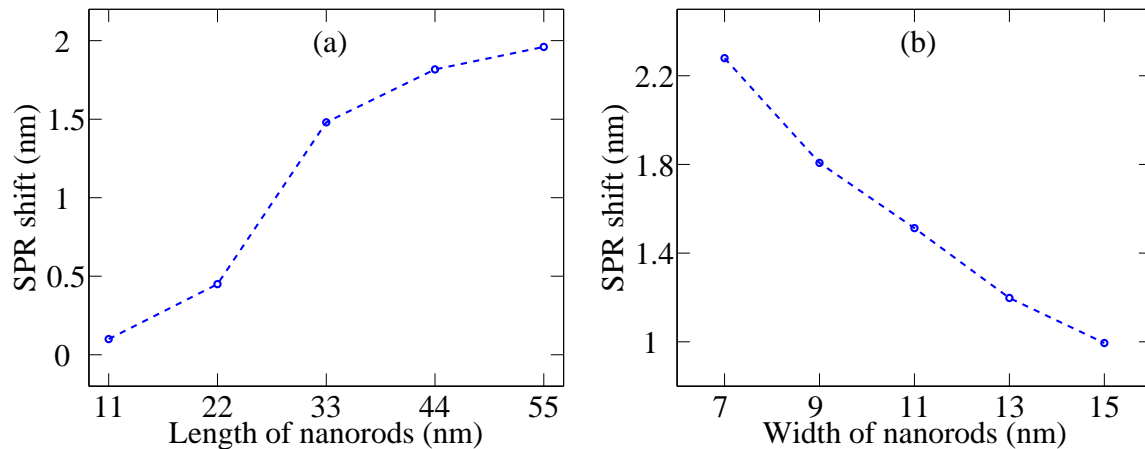


Figure 6.10: SPR shifts for an APC protein in response to TM incident light with different nanorod lengths (a) and widths (b).

## 6.3 Physical Orientation of Monomers in the Dimer

### 6.3.1 Nanorod Positions

Noble metal nanorods exhibit transverse and longitudinal plasmon modes corresponding to electron oscillation perpendicular and parallel to the length axis. The two modes individually define the plasmon coupling when the rods are positioned as side-by-side or linearly end-to-end orientation. However plasmon excitation simultaneously depends on these two modes when the rods are aligned at some angular orientation. Till date, a number of experiments and electrodynamic calculations have been performed on the plasmonic coupling of nanorod orientations [91]. Most of these studies have mainly focused on the dependence of the coupling strength on the spacing between metal nanorods [92–97]. But the dependence of the plasmon coupling on the inter-rod angle has rarely been explored. In this section, we have studied the angle-resolved plasmon coupling in Au@Ag dimers to find out its performance as biosensors. For this purpose, we have chosen a particular core-shell dimer structure with  $a_1 = 14.5$  nm,  $b_1 = 3.5$  nm, and  $d = 2$  nm. We have oriented the Au@Ag nanorod monomers at five different inclined angles  $\theta$ :  $60^\circ$ ,  $90^\circ$ ,  $120^\circ$ ,  $150^\circ$ , and  $180^\circ$ . We have analyzed the absorption spectrum of the proposed structure to the incident TM as well as TE polarized lights, which have been shown in Figs. 6.11(a) and 6.11(b) respectively. We note the absorption peak is found maximum at  $180^\circ$  of  $\theta$  for TM polarization, which executes a gradual decrease with descending values of  $\theta$ . On the contrary, TE incidence exhibits a progressive increase in absorption peaks for identical variation of  $\theta$

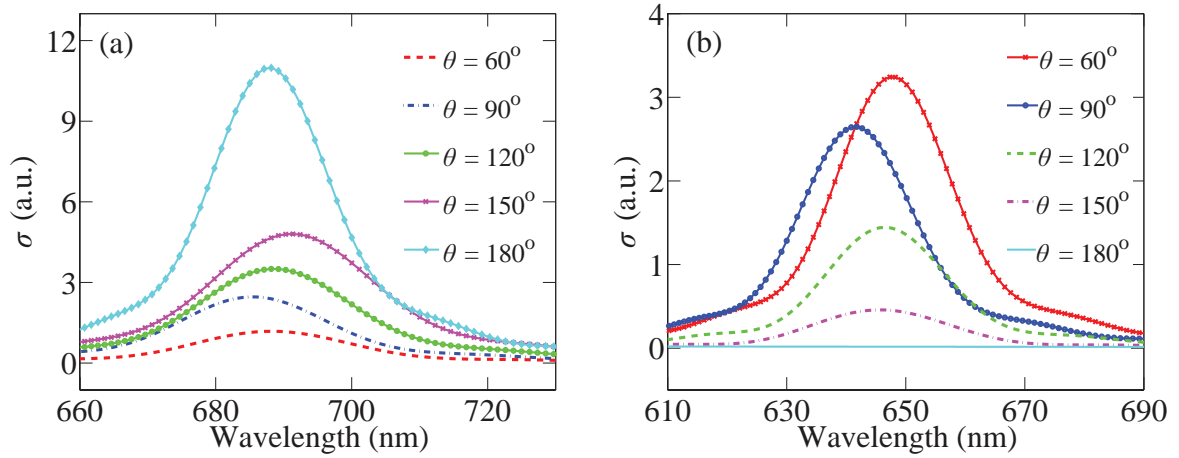


Figure 6.11: Absorption cross-section of the proposed dimer structure to the incident (a) TM and (b) TE polarized light at different angles between nanorods.

with almost zero absorption at  $180^\circ$  of  $\theta$ . These two opposite behaviors provide a reasonable explanation about the angle-resolved plasma coupling of the proposed system. The TM incident light produces longitudinal plasmon modes in longer resonant wavelengths (683 nm–686 nm) with the strongest coupling at  $180^\circ$  of  $\theta$ . The coupling weakens when the nanorods are brought closer with descending  $\theta$  values, resulting in lower absorption shown in Fig. 6.11(a). On the other hand, smaller values of  $\theta$  gradually increase the coupling along the transverse axis of the dimer when TE polarized light is incident, causing larger absorption in shorter wavelengths (643 nm–647 nm) shown in Fig. 6.11(b).

To have a more clearer view, we have calculated the electric field intensity ( $|E|$ ) for both TM and TE incidence at two different values of  $\theta$ . In Figs. 6.12(a) and 6.12(c) we provide the  $|E|$  profile at  $\theta = 120^\circ$ , whereas in Figs. 6.12(b) and 6.12(d) we show the  $|E|$  values at  $\theta = 60^\circ$ . If we look at Figs. 6.12(a) and 6.12(b), we can understand that the plasmon coupling due to TM incident light of 685 nm is stronger for higher values of  $\theta$  (closer to  $180^\circ$ ). However, opposite scenario is observed in Figs. 6.12(c) and 6.12(d), where TE polarized light of 647 nm produces stronger coupling for lower values of  $\theta$  (closer to  $0^\circ$ ). From these figures it is quite evident that TM incidence produces stronger coupling at the gap region than TE. So, nanorods aligned at  $180^\circ$  or near this angle is more preferred for biosensing than any other position.

With a view to verifying this conclusion, we have investigated the modeled dependence of resonant shifts due to APC protein on different nanorod positions. In Figs. 6.13(a) and 6.13(b) we present the shift dependence of proposed structure for

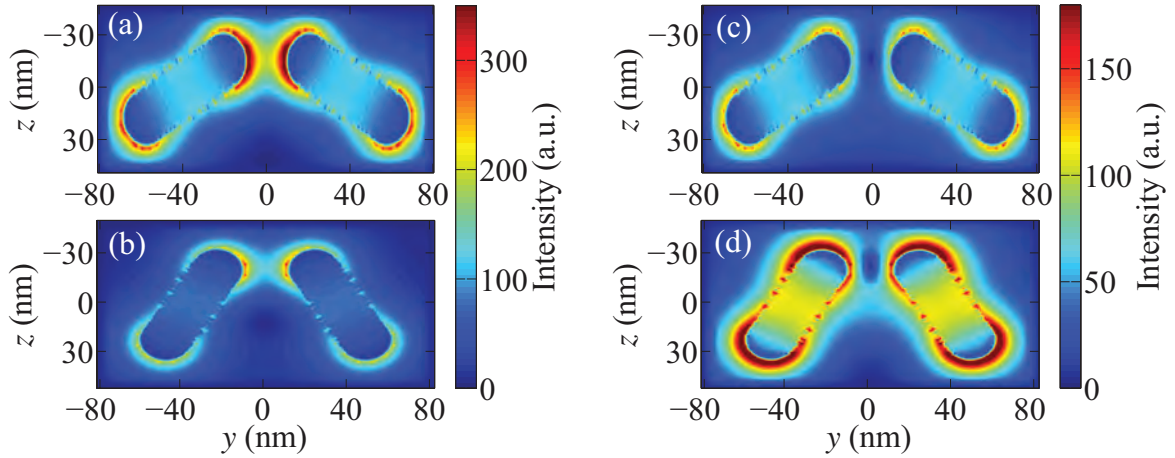


Figure 6.12: Response of the proposed dimer structure to the incident TM and TE polarized light at different angles between nanorods  $\theta$ : (a) Electric field intensity ( $|E|$ ) to the TM polarized light of 685nm at  $\theta = 120^\circ$ . (b) Electric field intensity ( $|E|$ ) to the TM polarized light of 685nm at  $\theta = 60^\circ$ . (c) Electric field intensity ( $|E|$ ) to the TE polarized light of 647nm at  $\theta = 120^\circ$ . (d) Electric field intensity ( $|E|$ ) to the TE polarized light of 647nm at  $\theta = 60^\circ$ .

TM and TE polarization respectively. In response to Fig. 6.13(a), we can find an approximately linear increase of SPR shifts ranging from 1.23 nm to 1.513 nm for nanorod orientations from  $60^\circ$  to  $180^\circ$ . This phenomenon completely agrees to the outcome we have found in Figs. 6.11 and 6.12. On the contrary, an almost linear decrease from 0.405 nm to 0.01 nm has been found for TE polarization with same nanorod positions in Fig. 6.13(b). Comparatively smaller shift values have been found in this case. The gradual decrease also verifies the idea found in Figs. 6.11 and 6.12. Therefore, the plasmonic sensitivity of the Au@Ag dimers can be estimated from Fig. 6.13 with different nanorod positions, which clearly verifies the preference of tip-to-tip orientation.

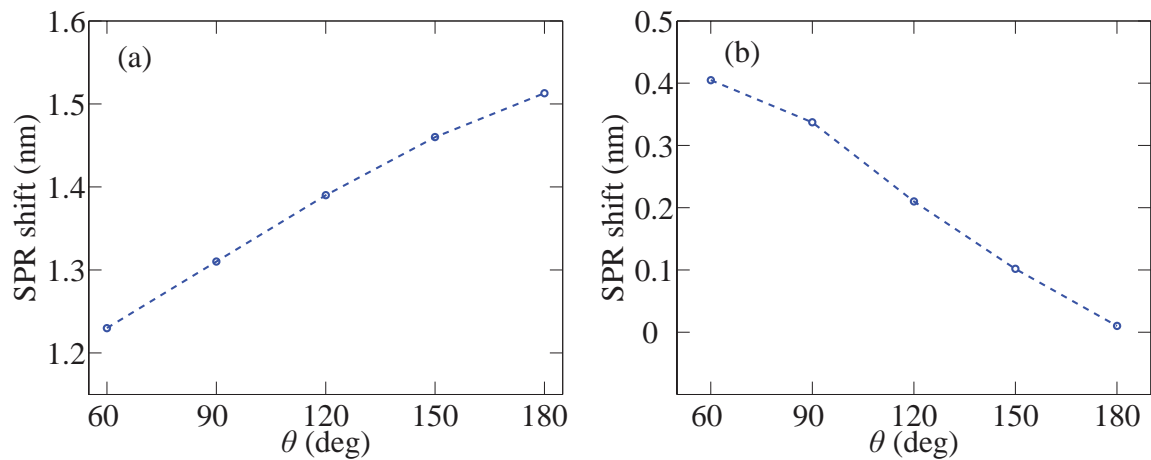


Figure 6.13: SPR shifts for an APC protein in response to TM (a) and TE (b) polarized light with different nanorod positions.

### 6.3.2 Gap Width between Nanorods

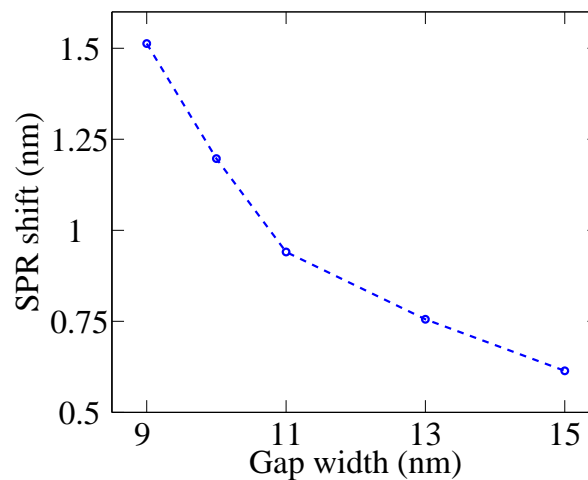


Figure 6.14: SPR shifts for an APC protein with different nanorod gap widths

In the presence of metal nanoparticles there is no fundamental limit preventing confinement of visible light even down to atomic scales. Achieving such confinement and corresponding intensity enhancement inevitably requires control over atomic-scale details of metal structures. In nanorod dimers, such control is mostly required across the gap between rod alignments where electric field confinement produces localized plasmon resonance. Variation of the gap width can strongly affect the plasmonic properties and hence bio-sensing performance of the dimer structure. With a view to investigating the modeled dependence of plasmonic sensitivity of the proposed bimetallic system, a detailed study has been undertaken with the model APC biosample. The SPR shifts

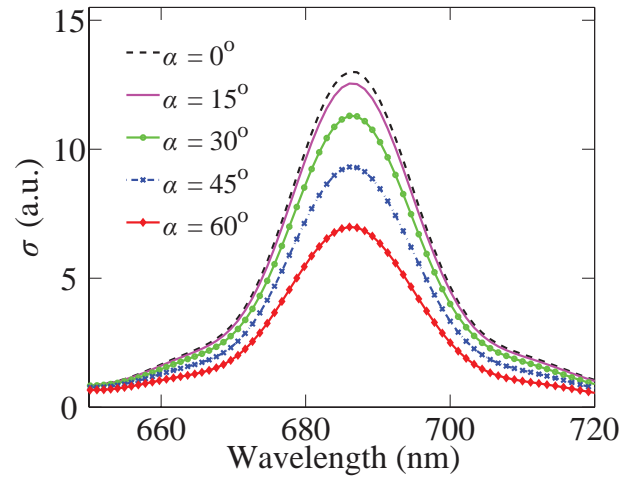


Figure 6.15: Absorption cross-section of the proposed dimer structure to the TM polarized light at different angles of incidence,  $\alpha$

have been calculated to the incident TM polarized light with variation of gap widths, which has been shown in Fig. 6.14. It is quite understandable that with the increase in gap width, the plasmon coupling would encounter a gradual weakening resulting in an exponential decrease in resonant shifts. Fig. 6.14 manifests this characteristic decay ranging from 1.513nm to 0.65nm for a gap increase from 9nm to 15nm. This behavior clearly explains the modeled dependence of SPR shifts in Au@Ag dimers on the gap width.

## 6.4 Parameters in Physical Environment

### 6.4.1 Incident Angle of Light

In practical experiments, it is quite impossible to always ensure the normal incidence of light onto the biosensing materials. The light can be incident at some different angles rather than at normal. In this section, we have investigated the SPR properties of the bimetallic system at different incident angles of light. For this study, we have chosen the proposed Au@Ag structure with  $a_1 = 14.5$  nm,  $b_1 = 3.5$  nm, and  $d = 2$  nm. We have analyzed the response of the proposed system to the TM polarized light at five incident angles  $\alpha$ :  $0^\circ$ ,  $15^\circ$ ,  $30^\circ$ ,  $45^\circ$ , and  $60^\circ$ . The angles have been measured with respect to x-axis, normal to the y-z substrate of the dimer. TE incidence has not been considered here due to the insignificant absorption and electric field coupling which would not change with  $\alpha$ . Having a look at the Fig. 6.15, we would find the resonant wavelength at 685 nm for all values of  $\alpha$ . The absorption peak ( $\sigma_{max}$ ) is maximum



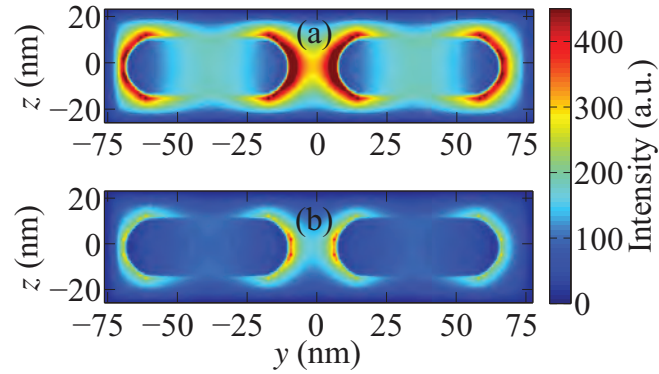


Figure 6.16: Electric field intensity ( $|E|$ ) to the TM polarized light of 685 nm at (a)  $\alpha = 0^\circ$  and (b)  $\alpha = 60^\circ$ .

at  $\alpha = 0^\circ$  and gradually reduces with the increase in  $\alpha$ . From this point of view, it is clear that the normal incident light would be the best option for biosensing. To have a more detailed study, we have calculated the electric field intensity ( $|E|$ ) of the bimetallic dimer at different angles of incidence.

Fig. 6.16(a) and Fig. 6.16(b) present the electric field profile at incident angles of  $0^\circ$  and  $60^\circ$  respectively. The incident TM polarized light strongly couples to plasmon excitation at resonant wavelength of 685 nm and produces higher values of  $|E|$  at incident angle of  $0^\circ$  rather than  $60^\circ$ . To highlight on this concept, we have calculated the resonant shifts for APC sample with respect to  $\alpha$  angles, which has been shown in Fig. 6.17. Maximum peak shift of 1.513 nm is found at  $0^\circ$  of  $\alpha$  which encounters a gradual decrease upto 1.139 nm when  $\alpha$  reaches at  $60^\circ$ . This observation clearly verifies the concept found in Fig. 6.16. So, at the end it can be concluded that the proposed structure would provide best bio-sensing performance at normal incident light.

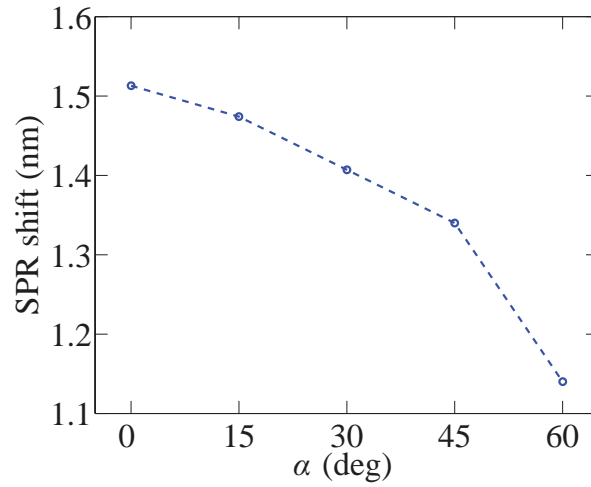


Figure 6.17: SPR shifts for an APC protein with different incident angles of light ( $\alpha$ ).

### 6.4.2 Chaotropic Agents in Buffer Solution

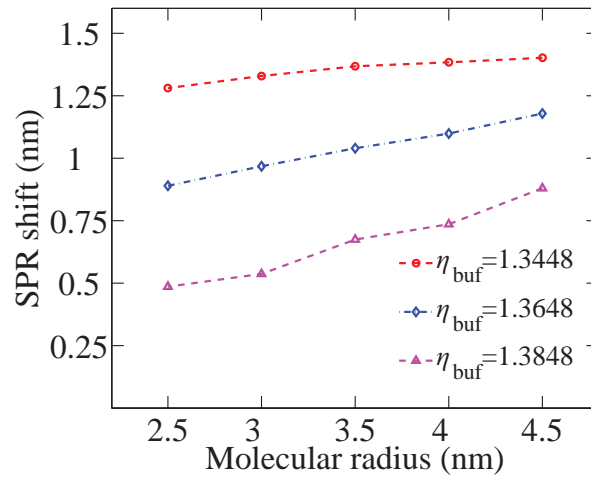


Figure 6.18: SPR shifts for denatured APC proteins with different chaotropic environment

Chaotropic agents are cosolutes that can disrupt the hydrogen bonding network between water molecules and reduce the stability of the native state of proteins by weakening the hydrophobic effect. Molecular denaturation of bioproteins due to chaotropic agents can lead to significant disruption in the SPR shifts and hence in plasmonic biosensing. In order to highlight on this phenomenon, the physical environment of the Au@Ag structure has been altered with chaotropic agents of different concentrations. Fig. 6.18 demonstrates the modeled dependence of the SPR shifts for denatured APC proteins with different chaotropic environments. TM polarization has

been used for plasmon excitation due to its better performance in bimetallic system. The Au@Ag nanorods have been chosen just as same as described in Sec. 6.4.1. The denaturization has been considered through gradual unfolding of the globular protein which has been modeled through continuous decrease in molecular radius along the longitudinal  $y$  axis. The chaotropic agent for our bimetallic structure has been chosen as urea, whose addition has led to an increase in the refractive index (RI) of the HEPES buffer. Greater molar concentrations of urea have been modeled through larger RI values of buffer solution. Moreover, conformational deformations of the protein sample has resulted in its gradual reduction in RI values which has been considered in a decay from 1.45 to 1.4. It can be noted from Fig. 6.18 that the conformational changes in the protein sample has led to an approximately linear decay in the SPR shifts. With lower concentration of urea ( $\eta_{\text{buf}} = 1.3448$ ), the decay is around 8.6%, whereas it increases upto 44.7% for higher molar concentration ( $\eta_{\text{buf}} = 1.3848$ ). So it can be concluded that denaturization of protein molecules due to chaotropic agents can result in significant degradation in SPR shifts and hence plasmonic sensitivity of the bimetallic system.

## 6.5 Sensitivity Analysis for Different Proteins

Proteins with significant biomarker applications have been chosen in this study. Chicken egg white lysozyme (Lys), human serum albumin (HSA), human  $\gamma$ -immunoglobulin (IgG), adenomatous polyposis coli (APC), and human fibrinogen (Fb) have been simulated on  $\text{SiO}_2$  between the gap of Au@Ag nanorods. The nanorod structure has been chosen at a particular core-shell ratio with  $a_1 = 14.5$  nm,  $b_1 = 3.5$  nm, and  $d = 2$  nm. With the proposed structure incident at TM polarized light, the SPR shifts for different protein molecules have been calculated to find out the molecular sensitivity of the bimetallic system.

### 6.5.1 Effects of Size and Material

With a view to presenting a complete scenario of the sensitivity of Au@Ag dimer sensor, the SPR shifts have been modeled for various sizes of proteins ranging from 14.3 kDa to 390 kDa. Fig. 6.19(a) provides a modeled dependence of resonance shifts on five different protein molecules placed in a fixed gap width of 9 nm between nanorods. On the other hand, the gap width has been varied in Fig. 6.19(b) to find out the maximum SPR shifts for the protein samples. From the two figures it is quite evident that the

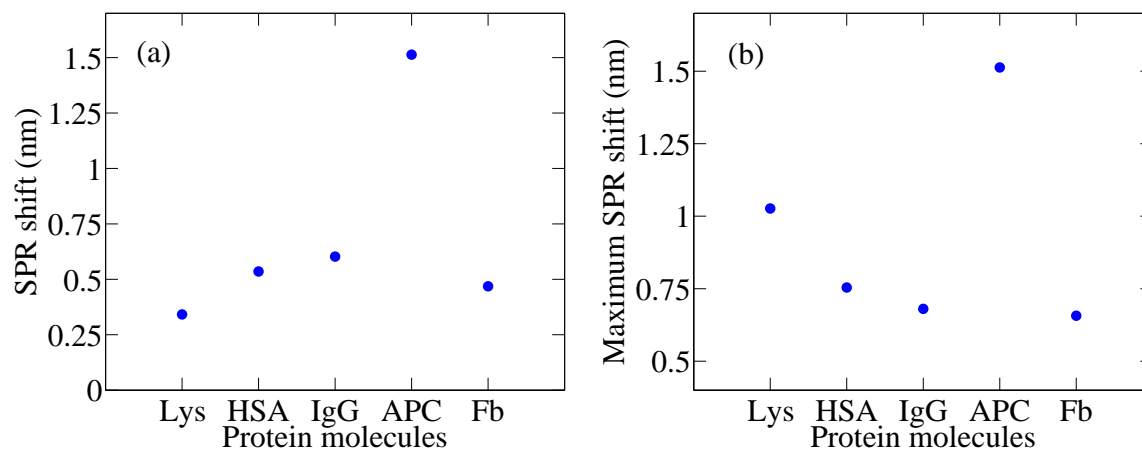


Figure 6.19: (a) SPR shifts for five bioproteins placed in a fixed gap width of 9 nm. (b) Maximum SPR shifts for the protein samples with optimized gap widths between nanorods.

resonance shifts are not only affected by molecular size but also by refractive index of proteins. These two parameters can dominate over each other depending on the physical situation of bimetallic nanorods. For example, in spite of having the highest refractive index (RI) of 1.5 among all the molecules, Lys executes the lowest SPR shift of 0.3416 nm in Fig. 6.19(a) due to its smaller globular size (14.3 kDa) placed in a fixed gap width of 9 nm. If the gap width could have been optimized in accordance with the size and shape of Lys, larger peak shifts of 1.0266 nm would have been observed just like Fig. 6.19(b). Furthermore, being the largest protein (390 kDa) among the samples, Fb exhibits comparatively smaller shift value of 0.4684 nm in Fig. 6.19(a). An elongated cylindrical shape and lowest RI value of 1.39 are the main factors behind this phenomenon. Larger resonant shift of 0.71 nm could have been found with Fb for optimized gap width, just as Fig. 6.19(b). HSA and IgG manifest almost identical peak shifts in both fixed and optimized gap widths, though the size and material of these samples are not same. Spherical IgG (140 kDa) is around two times larger than ellipsoidal HSA (66.5 kDa), but contains comparatively lower RI (1.41) material than HSA (1.45) which compensates for the size. The best performance is found for APC, which executes resonance shift of 1.513 nm in both Figs. 6.19(a) and 6.19(b). The protein provides the largest SPR shift among all the samples. A large globular size (275 kDa) and high RI material (1.46) has made it a perfect biosample for LSPR sensing.

### 6.5.2 Substrate Effect

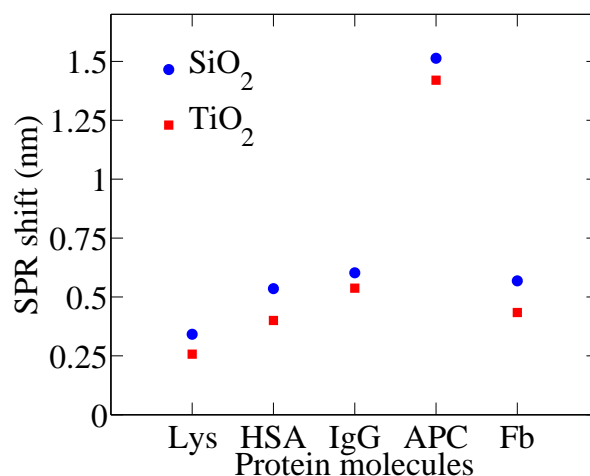


Figure 6.20: SPR shifts for different bioproteins with SiO<sub>2</sub> and TiO<sub>2</sub> substrates

The adsorption of proteins onto a plasmonic nanoparticle is usually a rapid process that within seconds generates a biologically active bond with the particle surface. The physical and chemical properties of the substrate may affect the protein adsorption and hence the plasmonic sensitivity of nanobiosensors. In Fig. 6.20, we have investigated the substrate effects on the sensitivity of the Au@Ag dimer for different protein molecules. We have studied two hydrophilic substrates, SiO<sub>2</sub> and TiO<sub>2</sub> which are extensively used in bio-sensing application. At both surfaces, the refractive index of all proteins are found to lie within 1.45–1.49. Having a look at Fig. 6.20, we can observe that the resonance shifts have been significantly decreased in case of TiO<sub>2</sub>, though it is more hydrophilic than SiO<sub>2</sub>. In practical case, TiO<sub>2</sub> executes around 82% higher refractive index than SiO<sub>2</sub> for different wavelengths of incident light. As a consequence, comparatively lower polarizability and hence electric field coupling is observed in a bimetallic nanorod sensor which in turn results in smaller SPR shifts for biosamples. In Fig. 6.20, around 24.7% decrement in resonance shift is observed for smaller protein like Lys, whereas 6.14% decrement is observed for larger protein like APC. From this analysis, it is quite obvious that substrate plays an important role in plasmonic sensitivity of Au@Ag sensors.

## 6.6 Summary

The main objective of the simulation was to investigate the molecular sensitivity of the proposed Au@Ag nanorod dimers in terms of SPR shifts. For this purpose, five different bioprotein samples were taken which have significant importance in biochemical and pharmaceutical applications. The plasmonic coupling of the proposed system was thoroughly investigated, which in turn provided a platform for bioprotein detection. After a systematic study, the bimetallic dimer was found to be more sensitive than the traditional Au structure. For better understanding, different parameter variation were investigated to observe the effects on the peak shifts for a model protein (APC) sample. This detailed analysis would give a valid estimation of the sensitivity efficiency of the proposed Au@Ag nanorod dimers for future experimental works.

# Chapter 7

## Conclusion and Future Works

This thesis work mainly focuses on the incorporation of LSPR in an Au@Ag nanorod dimer biosensor to explore its sensitivity in label-free molecule detection. Since Au and Ag have already been considered two of the most preferable options for LSPR, proper combination of these two metals is expected to introduce better and improved plasmonic properties for molecular sensitivity. In this thesis, we set some objectives to explore these properties in Au@Ag dimers through LSPR which were achieved and are discussed below:

- A detailed theoretical analysis of the Au@Ag nanorods has been performed at the beginning. Using the Clausius-Mossotti equation, an analytical model has been developed to discuss the optical properties, e.g., dielectric function of Au@Ag nanorod structure. The model has also been used to explain the plasmon resonance condition as well as the electron susceptibility of the bimetallic nanorod monomer.
- With the derived expressions for nanorod monomer, the optical polarizability and absorption cross-section of Au@Ag dimers have been calculated. Both bonding and antibonding plasmon modes of the absorption profile have been discussed for bimetallic as well as bare Au dimers. The discussion shows larger absorption spectra for the Au@Ag dimer than the conventional Au structure, which intrigues its possibility for biosensing applications.
- In order to further study the molecular sensitivity, the proposed bimetallic structure has been simulated without and with the presence of label-free proteins using the FDTD technique. Lysozyme (Lys), human serum albumin (HSA), human  $\gamma$ -immunoglobulin (IgG), adenomatous polyposis coli (APC) and human fibrinogen

(Fb) proteins have been used to calculate the resonance shifts from the FDTD simulations. The effects of size and material of these bioproteins placed in different substrates of the dimer sensor have been discussed in terms of SPR shifts of the absorption spectra.

- The effects of physical parameters, orientations and environment of the Au@Ag nanorods in the dimer structure have been studied through peak shifts for an APC protein sample. The absorption spectra and electric field coupling of the proposed bimetallic structure have been simulated to estimate the bio-sensitivity for different core-shell ratio, aspect ratio, nanorod positions, and incident angles of light. The gap width between nanorods have been varied to observe the effects on the SPR shifts. Moreover, denaturation of APC protein has been discussed in presence of chaotropic agents in the buffer solution.

It is quite obvious from our findings that the Au@Ag dimer provides much larger resonance shifts in presence of protein samples compared to the conventional Au dimer sensors. Therefore, the proposed bimetallic structure can be more suitable for LSPR biosensing applications in biomedical and pharmaceutical industries.

The next step of this work will be modification of the nanorod design in the Au@Ag dimer in order to explore the Fano Resonance for single molecule detection. Fano Resonance is considered a great possibility for bio-sensing applications and its incorporation in Au@Ag system will add massive contribution to our work.

In the future, we plan to experimentally verify the analytical and simulation results. The experimental verification of stronger electric field coupling and larger SPR shifts in label-free detection will provide validity to our works and broaden the research opportunities of Au@Ag nanorod dimers in biosensing as well as agricultural applications.



# Bibliography

- [1] Feynman, P. R., “There’s Plenty of Room at the Bottom,” *Caltech Engineering and Science*, vol. 23, pp. 22–36, 1960.
- [2] Stockman, M. I., “Nanoplasmonics: past, present, and glimpse into future,” *Optics Express*, vol. 19, pp. 22029–22106, 2011.
- [3] Giannini, V., Fernandez-Dominguez, A. I., Sonnefraud, Y., Roschuk, T., Fernandez-Garcia, R., and Maier, S. A., “Controlling Light Localization and Light-Matter Interactions with Nanoplasmonics,” *Small*, vol. 6, pp. 2498–2507, 2010.
- [4] Hutter, E. and Fendler, J. H., “Exploitation of localized surface plasmon resonance,” *Advanced Materials*, vol. 16, pp. 1685–1706, 2004.
- [5] Willets, K. A. and Van Duyne, R. P., “Localized surface plasmon resonance spectroscopy and sensing,” *Annual Review of Physical Chemistry*, vol. 58, pp. 267–297, 2007.
- [6] Lal, S., Link, S., and Halas, N. J., “Nano-optics from sensing to waveguiding,” *Nature Photonics*, vol. 1, pp. 641–648, 2007.
- [7] The British Museum, [http://www.britishmuseum.org/explore/highlights/highlight\\_objects/pe\\_mla/t/the\\_lycurgus\\_cup.aspx](http://www.britishmuseum.org/explore/highlights/highlight_objects/pe_mla/t/the_lycurgus_cup.aspx).
- [8] Brill, R. H., “The Chemistry of the Lycurgus Cup,” *Proc 7th Internat. Cong. Glass, comptes rendus 2*, paper 223, pp. 1–13, 1965.
- [9] Barber, D. J. and Freestone, I. C., “An investigation of the origin of the color of the lycurgus cup by analytical transmission electron-microscopy,” *Archaeometry*, vol. 32, pp. 33–45, 1990.

- [10] Hornyak, G. L., Patrissi, C. J., Oberhauser, E. B., Martin, C. R., Valmalette, J.-C., Lemaire, L., Dutta, J. and Hofmann, H., “Effective Medium Theory Characterization of Au/Ag Nanoalloy- porous Alumina Composites,” *NanoStructured Materials*, vol. 9, pp. 571–574, 1997.
- [11] Maier, S. A., Brongersma, M. L., Kik, P. G., Meltzer, S., Requicha, A. A. G., and Atwater, H. A., “Plasmonics - A route to nanoscale optical devices,” *Advanced Materials*, vol. 13, pp. 1501–1505, 2001.
- [12] Barnes, W. L., Dereux, A., and Ebbesen, T. W., “Surface plasmon subwavelength optics,” *Nature*, vol. 424, pp. 824–830, 2003.
- [13] Maier, S. A., Kik, P. G., and Atwater, H. A., “Observation of coupled plasmon-polariton modes in Au nanoparticle chain waveguides of different lengths: Estimation of waveguide loss,” *Applied Physics Letters*, vol. 81, pp. 1714–1716, 2002.
- [14] Atwater, H. A. and Polman, A., “Plasmonics for improved photovoltaic devices,” *Nature Materials*, vol. 9, pp. 205–213, 2010.
- [15] Wu, J. L., Chen, F. C., Hsiao, Y. S., Chien, F. C., Chen, P. L., Kuo, C. H., Huang, M. H., and Hsu, C. S., “Surface Plasmonic Effects of Metallic Nanoparticles on the Performance of Polymer Bulk Heterojunction Solar Cells,” *Acs Nano*, vol. 5, pp. 959–967, 2011.
- [16] Pillai, S., Catchpole, K. R., Trupke, T., and Green, M. A., “Surface plasmon enhanced silicon solar cells,” *Journal of Applied Physics*, vol. 8, pp. 101–106, 2007.
- [17] Christopher, P., Xin, H. L., and Linic, S., “Visible-light-enhanced catalytic oxidation reactions on plasmonic silver nanostructures,” *Nature Chemistry*, vol. 3, pp. 467–472, 2011.
- [18] Langhammer, C., Larsson, E. M., Kasemo, B., and Zoric, I., “Indirect Nanoplasmonic Sensing: Ultrasensitive Experimental Platform for Nanomaterials Science and Optical Nanocalorimetry,” *Nano Letters*, vol. 10, pp. 3529–3538, 2010.
- [19] Ankar, J. N., Hall, W. P., Lyandres, O., Shah, N. C., Zhao, J., and Van Duyne, R. P., “Biosensing with Plasmonic Nanosensors,” *Nature Materials*, vol. 7, pp. 442–453, 2008.

- [20] Jain, P. K., Huang, X. H., El-Sayed, I. H., and El-Sayed, M. A., “Noble Metals on the Nanoscale: Optical and Photothermal Properties and Some Applications in Imaging, Sensing, Biology, and Medicine,” *Accounts of Chemical Research*, vol. 41, pp. 1578–1586, 2008.
- [21] Sepulveda, B., Angelome, P. C., Lechuga, L. M., and Liz-Marzan, L. M., “LSPR-based nanobiosensors,” *Nano Today*, vol. 4, pp. 244–251, 2009.
- [22] Haes, A. J., Haynes, C. L., McFarland, A. D., Schatz, G. C., Van Duyne, R. R., and Zou, S. L., “Plasmonic materials for surface-enhanced sensing and spectroscopy,” *Mrs Bulletin*, vol. 30, pp. 368–375, 2005.
- [23] Yonzon, C. R., Stuart, D. A., Zhang, X. Y., McFarland, A. D., Haynes, C. L., and Van Duyne, R. P., “Towards advanced chemical and biological nanosensors - An overview,” *Talanta*, vol. 67, pp. 438–448, 2005.
- [24] Haes, A. J., Stuart, D. A., Nie, S. M., and Van Duyne, R. P., “Using solution-phase nanoparticles, surface-confined nanoparticle arrays and single nanoparticles as biological sensing platforms,” *Journal of Fluorescence*, vol. 14, pp. 355–367, 2004.
- [25] Szunerits, S. and Boukherroub, R., “Sensing using localised surface plasmon resonance sensors,” *Chemical Communications*, vol. 48, pp. 8999–9010, 2012.
- [26] Petryayeva, E. and Krull, U. J., “Localized surface plasmon resonance: Nanostructures, bioassays and biosensing-A review,” *Analytica Chimica Acta*, vol. 706, pp. 8–24, 2011.
- [27] Stewart, M. E., Anderton, C. R., Thompson, L. B., Maria, J., Gray, S. K., Rogers, J. A., and Nuzzo, R. G., “Nanostructured plasmonic sensors,” *Chemical Reviews*, vol. 108, pp. 494–521, 2008.
- [28] Haes, A. J., Hall, W. P., Chang, L., Klein, W. L., and Van Duyne, R. P., “A localized surface plasmon resonance biosensor: First steps toward an assay for Alzheimer’s disease,” *Nano Letters*, vol. 4, pp. 1029–1034, 2004.
- [29] Haes, A. J., Chang, L., Klein, W. L., and Van Duyne, R. P., “Detection of a biomarker for Alzheimer’s disease from synthetic and clinical samples using a nanoscale optical biosensor,” *Journal of the American Chemical Society*, vol. 127, pp. 2264–2271, 2005.

- [30] Acimovic, S. S., Ortega, M. A., Sanz, V., Berthelot, J., Garcia-Cordero, J. L., Renger, J., Maerkl, S. J., Kreuzer, M. P., and Quidant, R., “LSPR Chip for Parallel, Rapid, and Sensitive Detection of Cancer Markers in Serum,” *Nano Letters*, vol. 14, pp. 2636–2641, 2014.
- [31] Chen, H. J., Kou, X. S., Yang, Z., Ni, W. H., and Wang, J. F., “Shape- and size-dependent refractive index sensitivity of gold nanoparticles,” *Langmuir*, vol. 24, pp. 5233–5237, 2008.
- [32] Jain, P. K. and El-Sayed, M. A., “Plasmonic coupling in noble metal nanostructures,” *Chemical Physics Letters*, vol. 487, pp. 153–164, 2010.
- [33] Homola, J., Yee, S. S., and Gauglitz, G., “Surface plasmon resonance sensors: review,” *Elsevier Sensors and Actuators B Chemical*, vol.54, pp. 3–15, 1999.
- [34] Zijlstra, P., Paulo, P. M. R., and Orrit, M., “Optical detection of single non-absorbing molecules using the surface plasmon resonance of a gold nanorod,” *Nature Nanotechnology*, vol. 7, pp. 379–382, 2012.
- [35] Moerner, W. E. and Orrit, M., “Illuminating single molecules in condensed matter,” *Science*, vol. 283, pp. 1670–1676, 1999.
- [36] Kuhn, S., Hakanson, U., Rogobete, L., and Sandoghdar, V., “Enhancement of Single-Molecule Fluorescence Using a Gold Nanoparticle as an Optical Nanoantenna,” *Physics Review Letters*, vol. 97, art. 017402, 2006.
- [37] Dubertret, B., Calame, M., and Libchanber, A. J., “Single-mismatched detection using gold-quenched fluorescent oligoneucleotides,” *Nano Biotechnology*, vol. 19, pp. 365–370, 2001.
- [38] Wang, Z., Lee, J. H., and Lu, Y., “Label-Free Colorimetric Detection of Lead Ions with a Nanomolar Detection Limit and Tunable Dynamic Range by using Gold Nanoparticles and DNAzyme,” *Advanced Materials*, vol. 20, pp. 3263–3267, 2008.
- [39] Li, L., Lee, B., Qi, Y., and Jin, Y., “Label-free aptamer-based colorimetric detection of mercury ions in aqueous media using unmodified gold nanoparticles as colorimetric probe,” *Springer Analytical and Bioanalytical Chemistry*, vol. 393, pp. 2051–2057, 2009.

- [40] Ran, X., Sun, H., Pu, F., Ren, J., and Qu, X., “Ag Nanoparticle-decorated graphene quantum dots for label-free, rapid and sensitive detection of Ag<sup>+</sup> and biothiols,” *Chemical Communications*, vol. 49, pp. 1079–1081, 2013.
- [41] Mayer, K. M., and Hafner, J. H., “Localized surface plasmon resonance sensors,” *Chemical Review*, vol. 111, pp. 3828–3857, 2011.
- [42] Jia, K., Khaywah, M. Y., Li, Y., Bijeon, J. L., Adam, P. M., Deturche, R., Guelorget, B., Francois, M., Louarn, G., and Ionescu, R. E., “Strong Improvements of Localized Surface Plasmon Resonance Sensitivity by Using Au/Ag Bimetallic Nanostructures Modified with Polydopamine Films,” *ACS Applied Materials & Interface*, vol. 6, pp. 219–227, 2014.
- [43] Lumerical Solutions Inc., <http://www.lumerical.com/tcad-products/>.
- [44] Mie, G., “Beiträge zur Optik trüber Medien, speziell kolloidaler Metallösungen,” *Annalen der Physik*, vol. 330, is. 3, pp. 377–445, 1908.
- [45] Gans, R., “Über die Form ultramikroskopischer Goldteilchen,” *Annalen der Physik*, vol. 342, is. 5, pp. 881–900, 1912.
- [46] Dr. Bo Cui, <https://ece.uwaterloo.ca>.
- [47] Nano plasmon, <http://nanoplasmon.com/what-is-lspr>.
- [48] Johnson, P. B. and Christy, R. W., “Optical Constants of the Noble Metals,” *Physical Review B*, vol. 6, pp. 4370–4379, 1972.
- [49] Bohren, C. F. and Huffman, D.R., “Absorption and Scattering of Light by Small Particles,” *Wiley-Interscience*, New York, 1998.
- [50] Anderson, L. J. E., Mayer, K. M., Fraleigh, R. D., Yang, Y., Lee, S. and Hafner, J. H. J., “Quantitative Measurements of Individual Gold Nanoparticle Scattering Cross Sections,” *The Journal of Physical Chemistry C*, vol. 114, is. 25, pp. 11127–11132, 2010.
- [51] Eustis, S. and El-Sayed, M. A., “Determination of the aspect ratio statistical distribution of gold nanorods in solution from a theoretical fit of the observed inhomogeneously broadened longitudinal plasmon resonance absorption spectrum,” *Journal of Applied Physics*, vol. 100, art. 044324, 2006.

- [52] Link, S. and El-Sayed, M. A., "Simulation of the Optical Absorption Spectra of Gold Nanorods as a Function of Their Aspect Ratio and the Effect of the Medium Dielectric Constant," *The Journal of Physical Chemistry B*, vol. 109, is. 20, pp. 10531–10532, 2005.
- [53] Nehl, C. L. and Hafner, J. H., "Shape-dependent plasmon resonances of gold nanoparticles," *Journal of Material Chemistry*, vol. 18, pp. 2415–2419, 2008.
- [54] Mock, J. J., Barbic, M., Smith, D. R., Schultz, D. A., and Schultz, S., "Shape effects in plasmon resonance of individual colloidal silver nanoparticles," *Journal of Chemical Physics*, vol. 116, is. 15, pp. 6755–6759, 2002.
- [55] Grzelczak, M., Perez-Juste, J., Mulvaney, P., and Liz-Marzan, L. M., "Shape control in gold nanoparticle synthesis," *Chemical Society Reviews*, vol. 37, is. 9, pp. 1783–1791, 2008.
- [56] Daniel, M. C. and Astruc, D., "Gold nanoparticles: assembly, supramolecular chemistry, quantum-size-related properties, and applications toward biology, catalysis, and nanotechnology," *Chemical Reviews*, vol. 104, is. 1, pp. 293–346, 2004.
- [57] Lee, S. Y., Kim, S. H., Jang, S. G., Heo, C. J., Shim, J. W., and Yang, S. M., "High-Fidelity Optofluidic On-Chip Sensors Using Well-Defined Gold Nanowell Crystals," *Analytical Chemistry*, vol. 83, is. 23, pp. 9174–9180, 2011.
- [58] Corbierre, M. K., Beerens, J., Beauvais, J., and Lennox, R. B., "Uniform One-Dimensional Arrays of Tunable Gold Nanoparticles with Tunable Interparticle Distances," *Chemistry of Materials*, vol. 18, is. 11, pp. 2628–2631, 2006.
- [59] Vedantam, P., Tzeng, T. R. J., Brown, A. K., Podila, R., Rao, A., and Staley, K., "Binding of Escherichia coli to Functionalized Gold Nanoparticles," *Plasmonics*, vol. 7, is. 2, pp. 301–308, 2012.
- [60] Rycenga, M., Cobley, C. M., Zeng, J., Li, W. Y., Moran, C. H., Zhang, Q., Qin, D., and Xia, Y. N., "Controlling the Synthesis and Assembly of Silver Nanostructures for Plasmonic Applications," *Chemical Reviews*, vol. 111, is. 6, pp. 3669–3712, 2011.
- [61] Wang, H. H., Liu, C. Y., Wu, S. B., Liu, N. W., Peng, C. Y., Chan, T. H., Hsu, C. F., Wang, J. K., and Wang, Y. L., "Highly Raman-Enhanced Substrates Based on

- Silver Nanoparticles Arrays with Tunable Sub-10 nm Gaps,” *Advanced Materials*, vol. 18, is. 4, pp. 491–495, 2006.
- [62] Feng, C., Xu, G., Liu, H., Lv, J., Zheng, Z., and Wu, Y., “Glucose biosensors based on Ag nanoparticles modified TiO<sub>2</sub> nanotube arrays,” *Journal of Solid State Electrochemistry*, vol. 18, is. 1, pp. 163–171, 2013.
- [63] Liu, C. H., Li, Z. P., Du, B. A., Duan, X. R., and Wang, Y. C., “Silver Nanoparticle-Based Ultrasensitive Chemiluminescent Detection of DNA Hybridization and Single-Nucleotide Polymorphisms,” *Analytical Chemistry*, vol. 78, is. 11, pp. 3738–3744, 2006.
- [64] Behrens, S., Wu, J., Habicht, W., and Unger, E., “Silver Nanoparticle and Nanowire Formation by Microtubule Templates,” *Chemistry of Materials*, vol. 16, is. 16, pp. 3085–3090, 2004.
- [65] Willets, K. A. and Van Duyne, R. P., “Localized Surface Plasmon Resonance Spectroscopy and Sensing,” *Annual Review of Physical Chemistry*, vol. 58, pp. 267–297, 2007.
- [66] El-Sayed, M. A., “Some Interesting Properties of Metals Confined in Time and Nanometer Space of Different Shapes,” *Accounts of Chemical Research*, vol. 34, is. 4, pp. 257–264, 2001.
- [67] Michaels, A. M., Nirmal, M., and Brus, L. E. J., “Some Interesting Properties of Metals Confined in Time and Nanometer Space of Different Shapes,” *Accounts of Chemical Research*, vol. 34, is. 4, pp. 257–264, 2001.
- [68] Kelly, K. L., Coronado, E., Zhao, L. L., and Schatz, G. C., “The Optical Properties of Metal Nanoparticles : The Influence of Size, Shape, and Dielectric Environment,” *The Journal of Physical Chemistry B*, vol. 107, is. 3, pp. 668–677, 2003.
- [69] Smitha, S. L., Gopchandran, K. G., Ravindran, T. R., and Prasad, V. S., “Gold nanorods with finely tunable longitudinal surface plasmon resonance as SERS substrates,” *Nanotechnology*, vol. 22, num. 26, 2011.
- [70] Mayer, K. M. and Hafner, J. H., “Localized Surface Plasmon Resonance Sensors,” *Chemical Reviews*, vol. 111, is. 6, pp. 3828–3857, 2011.

- [71] Szunzerits, S. and Boukherroub, R., “Sensing using localised surface plasmon resonance sensors,” *Chemical Communications*, vol. 48, pp. 8999–9010, 2012.
- [72] Yanik, A. A., Cetin, A. E., Huang, M., Artar, A., Mousavi, S. H., Khanikaev, A., Connor, J. H., Shvets, G., and Altug, H., “Sensing using localised surface plasmon resonance sensors,” *Proceedings of the National Academy of Sciences of the United States of America*, vol. 108, pp. 11784–11789, 2011.
- [73] Choi, I., Song, H. D., Lee, S., Yang, Y. I., Kang, T., and Yi, J. J., “Core–Satellites Assembly of Silver Nanoparticles on a Single Gold Nanoparticle via Metal Ion-Mediated Complex,” *Journal of the American Chemical Society*, vol. 134, pp. 12083–12090, 2012.
- [74] Dreaden, E. C., Alkilany, A. M., Huang, X. H., Murphy, C. J., and ElSayed, M. A., “The golden age: gold nanoparticles for biomedicine,” *Chemical Society Reviews*, vol. 41, pp. 2740–2779, 2012.
- [75] Huang, X. H., El-Sayed, I. H., Qian, W., and El-Sayed, M. A., “Cancer Cell Imaging and Photothermal Therapy in the Near-Infrared Region by Using Gold Nanorods,” *Journal of the American Chemical Society*, vol. 128, pp. 2115–2120, 2006.
- [76] Oulton, R. F., Sorger, V. J., Genov, D. A., Pile, D. F. P., and Zhang, X., “A hybrid plasmonic waveguide for subwavelength confinement and long-range propagation,” *Nature Photonics*, vol. 2, pp. 496–500, 2008.
- [77] Dragoman, M. and Dragoman, D., “Plasmonics: Applications to nanoscale terahertz and optical devices,” *Progress in Quantum Electronics*, vol. 32, pp. 1–41, 2008.
- [78] Kneipp, K., Wang, Y., Kneipp, H., Perelman, L. T., Itzkan, I., Dasari, R. R., and Feld, M. S., “Single Molecule Detection Using Surface-Enhanced Raman Scattering (SERS),” *Physical Review Letters*, vol. 78, pp. 1667–1670, 1997.
- [79] Aslan, K. and Geddes, C. D., “Directional Surface Plasmon Coupled Luminescence for Analytical Sensing Applications: Which Metal, What Wavelength, What Observation Angle?,” *Analytical Chemistry*, vol. 81, pp. 6913–6922, 2009.



- [80] Halas, N. J., Lal, S., Chang, W. S., Link, S., and Nordlander, P., “Plasmons in Strongly Coupled Metallic Nanostructures,” *Chemical Reviews*, vol. 111, pp. 3913–3961, 2011.
- [81] Wu, J., Lu, X., Zhu, Q., Zhao, J., Shen, Q., and Zhan, L., “Angle-resolved Plasmonic Properties of Single Gold Nanorod Dimers,” *Nano-Micro Letters*, vol. 6, is. 4, pp. 372–380, 2014.
- [82] Makarov, D. V., Loeb, S., Getzenberg, R. H., and Partin, A. W., “Biomarkers for prostate cancer,” *Annual Review Medicine*, vol. 60, pp. 139–151, 2009.
- [83] Ramm, A. G., “Iterative Methods for Calculating the Static Fields and Wave Scattering by Small Bodies,” *Springer Verlag*, New York, 1982.
- [84] Ramm, A. G., “Wave Scattering by Small Bodies of Arbitrary Shapes,” *World Sci. Publishers*, Singapore, 2005.
- [85] Ahmed, S., Wang, W., Bai, L., Gentekos, D. T., Hoyos, M., and Mallouk, T. E., “Density and Shape Effects in the Acoustic Propulsion of Bimetallic Nanorod Motors,” *ACS Nano*, vol. 10, is. 4, pp. 4763–4769, 2016.
- [86] Rayleigh, D. W., “On the incident of aerial and electric waves upon small obstacles in the form of ellipsoids or elliptical cylinders, and on the passage of electric waves through a circular aperture in a conducting screen,” *Phil. Mag.*, vol. 44, is. 266, pp. 28–52, 1897.
- [87] Johnson, P. B. and Christy, R. W., “Optical Constants of the Noble Metals,” *Physics Review B*, vol. 6, no. 12, 1972.
- [88] Shao, L., Woo, K. C., Chen, H., Jin, Z., Wang, J., and Lin, H. Q., “Angle- and Energy-Resolved Plasmon Coupling in Gold Nanorod Dimers,” *ACS Nano*, vol. 4, no. 6, 2010.
- [89] Voros, J., “The Density and Refractive Index of Adsorbing Protein Layers,” *Elsevier Biophysical Journal*, vol. 87, is. 1, pp. 553–561, 2004.
- [90] Erickson, H. P., “Size and Shape of Protein Molecules at the Nanometer Level Determined by Sedimentation, Gel Filtration, and Electron Microscopy,” *Biological Procedures Online*, vol. 11, no. 1, pp. 32–51, 2009.

- [91] Ghosh, S. K. and Pal, T., “Interparticle Coupling Effect on the Surface Plasmon Resonance of Gold Nanoparticles: From Theory to Applications,” *Chemical Reviews*, vol. 107, pp. 4797–4862, 2007.
- [92] Jain, P. K., Eustis, S., and El-Sayed, M. A., “Plasmon Coupling in Nanorod Assemblies: Optical Absorption, Discrete Dipole Approximation Simulation, and Exciton-Coupling Model,” *Journal of Physical Chemistry B*, vol. 110, pp. 18243–18253, 2006.
- [93] Willingham, B., Brandl, D. W., and Nordlander, P., “Plasmon Hybridization in Nanorod Dimers,” *Applied Physics B: Lasers and Optics*, vol. 93, pp. 209–216, 2008.
- [94] Sun, Z. H., Ni, W. H., Yang, Z., Kou, X. S., Li, L., and Wang, J. F., “pH-Controlled Reversible Assembly and Disassembly of Gold Nanorods,” *Small*, vol. 4, pp. 1287–1292, 2008.
- [95] Tabor, C., Van Haute, D., and El-Sayed, M. A., “Effect of Orientation on Plasmonic Coupling between Gold Nanorods,” *ACS Nano*, vol. 3, pp. 3670–3678, 2009.
- [96] Funston, A. M., Novo, C., Davis, T. J., and Mulvaney, P., “Plasmon Coupling of Gold Nanorods at Short Distances and in Different Geometries,” *Nano Letters*, vol. 9, pp. 1651–1658, 2009.
- [97] Verellen, N., Sonnefraud, Y., Sobhani, H., Hao, F., Moshchalkov, V. V., Dorpe, P. V., Nordlander, P., and Maier, S. A., “Fano Resonances in Individual Coherent Plasmonic Nanocavities,” *Nano Letters*, vol. 9, pp. 1663–1667, 2009.